

IMMUNOTHERAPY

PD-1 blockade exacerbates *Mycobacterium tuberculosis* infection in rhesus macaques

Keith D. Kauffman¹, Shunsuke Sakai¹, Nickiana E. Lora¹, Sivaranjani Namasivayam², Paul J. Baker³, Olena Kamenyeva⁴, Taylor W. Foreman¹, Christine E. Nelson¹, Deivide Oliveira-de-Souza⁵, Caian L. Vinhaes⁵, Ziv Yaniv⁶, Cecilia S. Lindestam Arleham⁷, Alessandro Sette^{7,8}, Gordon J. Freeman⁹, Rashida Moore¹⁰, NIAID/DIR Tuberculosis Imaging Program*, Alan Sher², Katrin D. Mayer-Barber³, Bruno B. Andrade⁵, Juraj Kabat⁴, Laura E. Via^{11*}, Daniel L. Barber^{1†}

Copyright © 2021
The Authors, some
rights reserved;
exclusive licensee
American Association
for the Advancement
of Science. No claim
to original U.S.
Government Works

Boosting immune cell function by targeting the coinhibitory receptor PD-1 may have applications in the treatment of chronic infections. Here, we examine the role of PD-1 during *Mycobacterium tuberculosis* (Mtb) infection of rhesus macaques. Animals treated with anti-PD-1 monoclonal antibody developed worse disease and higher granuloma bacterial loads compared with isotype control-treated monkeys. PD-1 blockade increased the number and functionality of granuloma Mtb-specific CD8 T cells. In contrast, Mtb-specific CD4 T cells in anti-PD-1-treated macaques were not increased in number or function in granulomas, expressed increased levels of CTLA-4, and exhibited reduced intralosomal trafficking in live imaging studies. In granulomas of anti-PD-1-treated animals, multiple proinflammatory cytokines were elevated, and more cytokines correlated with bacterial loads, leading to the identification of a role for caspase 1 in the exacerbation of tuberculosis after PD-1 blockade. Last, increased Mtb bacterial loads after PD-1 blockade were found to associate with the composition of the intestinal microbiota before infection in individual macaques. Therefore, PD-1-mediated coinhibition is required for control of Mtb infection in macaques, perhaps because of its role in dampening detrimental inflammation and allowing for normal CD4 T cell responses.

INTRODUCTION

Mycobacterium tuberculosis (Mtb) infection is the leading cause of death due to a single infectious agent worldwide, despite the availability of antibiotics that can effectively treat most Mtb infections (1). Drugs that target the host rather than the bacteria, i.e., host-directed therapies (HDTs), may be useful in shortening the standard 6-month-long course of antibiotic treatment, as well as providing sorely needed new options for the treatment of drug resistant infections (2–4). In particular, there is interest in developing strategies to boost host-protective immune responses or on the other hand limiting the detrimental inflammation that causes tissue destruction and promotes bacterial growth during tuberculosis (TB). However, the mecha-

nisms of host resistance and tissue pathology during Mtb infection are incompletely understood, impeding the development of HDTs.

PD-1 (programmed death-1) is a coinhibitory receptor primarily expressed on activated CD4 and CD8 T cells that has been shown to limit the function of pathogen-specific T cells during chronic infection and tumor-specific T cells during cancer (5, 6). Blockade of PD-1 or its ligands with monoclonal antibodies (mAbs) enhances the number and function of antitumor cytotoxic T cells resulting in enhanced tumor control, and there are multiple PD-1-targeting drugs approved for use against various malignancies (6). The major success of immune checkpoint blockade-targeting drugs in cancer treatment has highlighted how potent such approaches can be in the treatment of human disease. Boosting T cell function by blocking PD-1 has been suggested as a therapy for TB (7).

Human Mtb-specific T cells in circulation can express low levels of PD-1 during disease, and in vitro blockade of PD-1 can enhance T cell responses, although the effects are modest (8). The first in vivo data on the role of PD-1 in Mtb infection came from knockout (KO) mouse studies where it was found that PD-1^{-/-} mice die very rapidly after Mtb infection compared with wild-type (WT) mice (9, 10). In the absence of PD-1, CD4 T cells and, to a lesser extent, CD8 T cells drive this early mortality (10). Although the T cell mechanisms that cause pathology in Mtb-infected PD-1^{-/-} mice are not completely understood, we have shown that the overproduction of interferon- γ (IFN γ) by CD4 T cells is at least partly responsible (11), and in a human in vitro three-dimensional (3D) granuloma model, it was found that PD-1 blockade drives higher bacterial loads in a tumor necrosis factor (TNF)-dependent manner (12). Consistent with these data showing a host-protective role for PD-1 in Mtb infection, clinical case reports of checkpoint blockade-associated TB in patients treated with anti-PD-1 (α PD-1) are accumulating in the literature (12–18).

¹T Lymphocyte Biology Section, Laboratory of Parasitic Diseases, National Institute of Allergy and Infectious Diseases, National Institutes of Health, Bethesda, MD, USA. ²Immunobiology Section, Laboratory of Parasitic Diseases, National Institute of Allergy and Infectious Diseases, National Institutes of Health, Bethesda, MD, USA. ³Inflammation and Innate Immunity Unit, Laboratory of Clinical Immunology and Microbiology, National Institute of Allergy and Infectious Diseases, National Institutes of Health, Bethesda, MD, USA. ⁴Biological Imaging Section, Research Technologies Branch, National Institute of Allergy and Infectious Diseases, National Institutes of Health, Bethesda, MD, USA. ⁵Multinational Organization Network Sponsoring Translational and Epidemiological Research (MONSTER) Initiative, Instituto Gonçalo Moniz, Fundação Oswaldo Cruz, Salvador, Brazil. ⁶Office of Cyber Infrastructure and Computational Biology, National Institute of Allergy and Infectious Diseases, National Institutes of Health, Bethesda, MD, USA. ⁷Division of Vaccine Discovery, La Jolla Institute for Immunology, La Jolla, CA, USA. ⁸Department of Medicine, University of California, San Diego, La Jolla, CA, USA. ⁹Department of Medical Oncology, Dana-Farber Cancer Institute, Harvard Medical School, Boston, MA, USA. ¹⁰Comparative Medicine Branch, National Institute of Allergy and Infectious Diseases, National Institutes of Health, Bethesda, MD, USA. ¹¹Tuberculosis Research Section, Laboratory of Clinical Infectious Diseases, National Institute of Allergy and Infectious Diseases, National Institutes of Health, Bethesda, MD, USA. *The members of the NIAID/DIR Tuberculosis Imaging Program can be found at the end of the Acknowledgments.

†Corresponding author. Email: barberd@niaid.nih.gov

Mycobacterium avium infections have also been observed in individuals undergoing PD-1 blockade cancer immunotherapy (19). This has led to the hypothesis that the negative regulation of T cells through PD-1 is required for optimal control of Mtb infection, perhaps by the inhibition of detrimental hyperinflammatory T cell responses. However, because of the caveats inherent to the murine model of TB and the anecdotal nature of the published case reports, the role of PD-1 in host resistance to Mtb infection *in vivo* has yet to be definitively addressed.

Macaques are considered the gold standard preclinical model of Mtb infection, because they very accurately recapitulate many features of human TB pathogenesis and immune responses against the pathogen (20). Therefore, in the current study, we treated Mtb-infected rhesus macaques with α PD-1 to examine the role of this clinically important regulatory pathway during TB. We found that PD-1 blockade drove higher levels of inflammation and increased bacterial loads in pulmonary granulomas. Together with the previously published data, these results strongly indicate that, somewhat counterintuitively, the coinhibitory receptor PD-1 is host protective during Mtb infection and that negative immune regulation is an important aspect of host resistance during TB.

RESULTS

Increased bacterial loads after PD-1 blockade

To examine the levels of PD-1 expression by T cells in different tissues, rhesus macaques were infected with Mtb and tissues harvested 15 to 16 weeks after infection. PD-1 expression was most highly expressed on antigen (Ag)-specific CD4 and CD8 T cells in lung granulomas compared with other tissues, including the blood and even the bronchoalveolar lavage (BAL) (Fig. 1, A and B). In granulomas, PD-1 staining was largely restricted to the peripheral lymphocyte-rich cuff (Fig. 1C) and was detectable on CD4⁺ and CD8⁺ cells (Fig. 1D). Therefore, PD-1 is preferentially expressed on Mtb-specific T cells in pulmonary granulomas, the primary site of bacterial replication.

To examine the role of PD-1 during Mtb infection, macaques were treated with a primatized α PD-1-blocking mAb or rhesus macaque isotype control mAb starting 2 weeks after infection (Fig. 2A). We chose to start treatment at 2 weeks after infection to allow for a normal course of infection for most of the time before induction of adaptive immunity. Our hypothesis was that PD-1 blockade would impair control of the infection. Accordingly, a dose and strain of Mtb was chosen that, in our experience, results in a slowly progressive course of infection, so that the virulence of the bacteria would not mask the predicted effect of PD-1 blockade.

All six isotype control-treated animals survived until the predetermined end point (weeks 15 to 16), displayed no signs of weight loss and had stable disease as measured by ¹⁸FDG (fluorodeoxyglucose)-positron emission tomography (PET)-computed tomography (CT) imaging (Fig. 2, B to D). In contrast, one of the α PD-1-treated animals (DGOi) developed acute symptoms and was euthanized early, another developed cachexia and relatively elevated ¹⁸FDG uptake but survived until the study end (DG9R), and yet another displayed higher PET-CT scores but did not lose weight (DGKA) (Fig. 2, B to D). Upon necropsy, we found that isotype control- and α PD-1-treated animals had similar numbers of granulomas, but the granulomas in α PD-1-treated macaques were larger (Fig. 2, E and F). α PD-1-treated macaques had an ~20-fold increase in the numbers of bacteria in their granulomas relative to animals treated with isotype control mAb (Fig. 2G). Whereas four of the six α PD-1-treated macaques displayed increased bacterial loads, two animals (DG3X and DG2T) were “nonresponders” and had low bacterial loads similar to the isotype control-treated animals. Although the bacterial loads were similar in the lung-draining lymph nodes, a higher percentage of pulmonary lymph nodes were infected in the α PD-1-treated group compared with control macaques, and most spleen samples did not contain bacteria (Fig. 2, H and I).

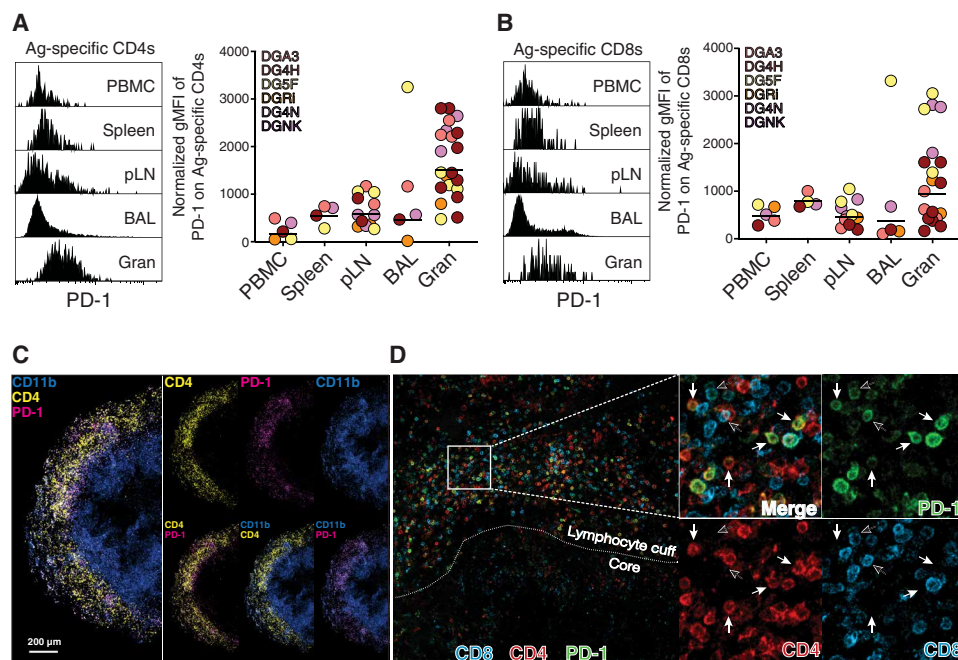


Fig. 1. PD-1 expression is highest on T cells in pulmonary granulomas. (A and B) Example histograms and summary graphs of PD-1 staining by flow cytometry on (A) CD4 T cells and (B) CD8 T cells from the indicated tissues at necropsy, ~15 weeks after infection with 30 to 50 CFU of H37Rv-mCherry. Mtb-specific T cells were identified as TNF⁺ by intracellular cytokine staining after stimulation with a combination of CD4 and CD8 T cell Mtb peptide megapools. The normalized geometric mean fluorescent intensity (geoMFI) was calculated by subtracting the geoMFI of PD-1-negative T cells in blood of the same animal from the TNF⁺ Ag-specific T cells in different tissues. pLN, pulmonary lymph node. (C) PD-1 (magenta), CD4 (yellow), and CD11b (blue) staining in an Mtb granuloma. Left image is merged and smaller images on right show individual staining (top) and two-stain combinations (bottom). Image is from animal DG4H. Note that the mCherry signal was undetectable at this time point. (D) Costaining of PD-1 (green), CD4 (red), and CD8 (blue) in a granuloma. Left image is merged and shows the boundary of the lymphocyte cuff and core. Expanded image shows individual stains and merged image. White arrows indicate PD-1⁺CD4⁺ cells, and black arrows indicate PD-1⁺CD8⁺ cells. This image from animal MFN is from a separate infection (5 weeks after infection with 12 to 14 CFU Mtb-Erdman) and is included because CD8 staining in granulomas was not performed in PD-1 blockade study.

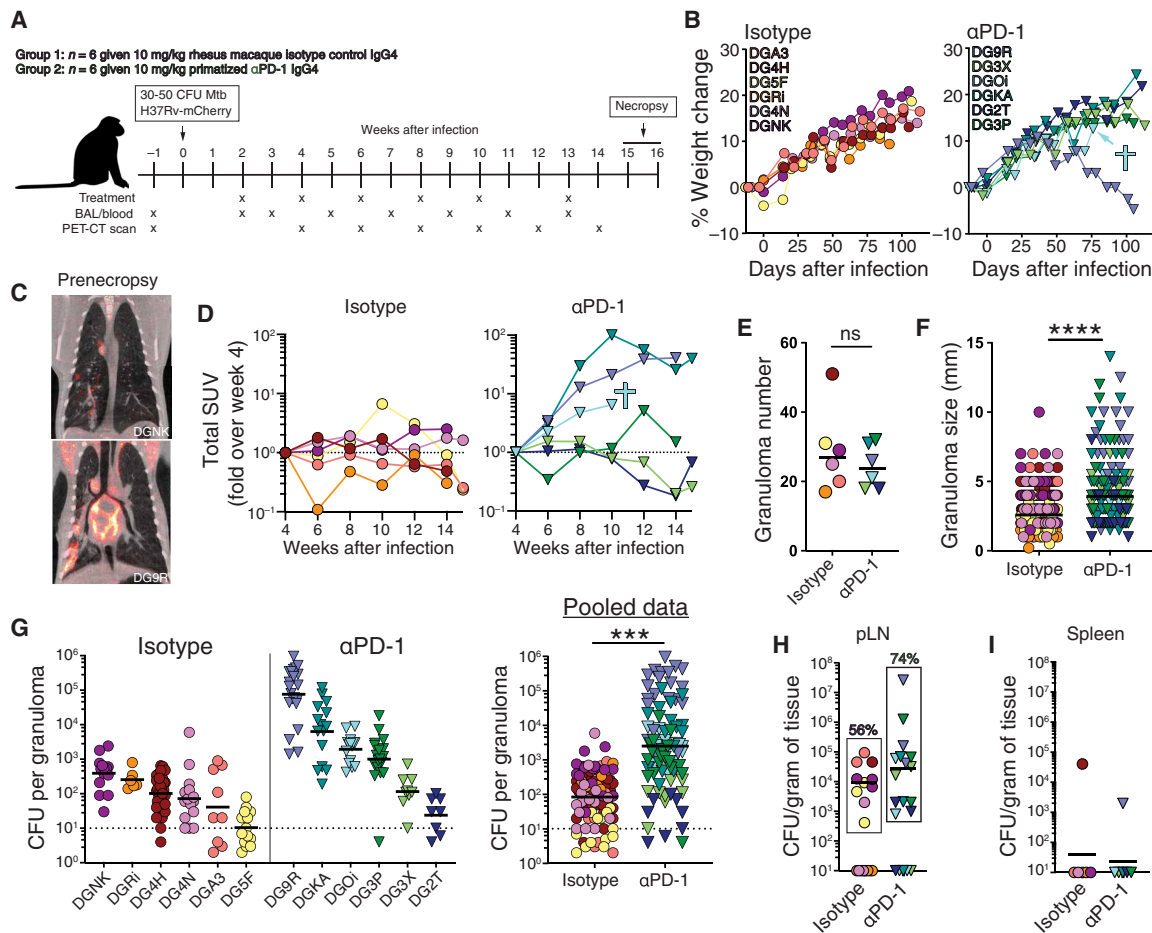


Fig. 2. PD-1 blockade exacerbates TB in macaques. (A) Twelve animals were infected with 30 to 50 CFU of H37Rv-mCherry. Starting 2 weeks after infection, animals were treated with a rhesus macaque IgG4 isotype control ($n=6$) or a primatized α PD-1 mAb ($n=6$). Animals were necropsied at week 15 or 16 after infection. (B) Weight change of animals receiving isotype control (left) and α PD-1 (right). Blue cross indicates euthanasia of DGOi before study due to the development of severe pulmonary distress. (C) Example PET-CT image from isotype control– (top) or α PD-1 (bottom)–treated animals. (D) Fold change over week 4 value of total lung standardized uptake value (SUV) in isotype control (left) and α PD-1–treated (right) animals. (E) At necropsy, the entire lung was closely examined, and all granulomas were isolated. Graph represents the number of granulomas recovered from the whole lung. ns, not significant. (F) Diameter of each granuloma was measured at necropsy. Average of two perpendicular measurements was taken for irregularly shaped lesions. (G) Bacterial loads in granulomas displayed in individual animals (left) or pooled by experimental group (right). Each dot represents an individual granuloma. Dotted line indicates limit of detection. (H and I) Bacterial burden in (H) pulmonary lymph nodes and (I) spleen. Percentage of total lymph nodes from each experimental group that had positive bacterial cultures is indicated. * $P < 0.05$, ** $P < 0.01$, *** $P < 0.001$, and **** $P < 0.0001$.

Thus, PD-1 blockade increased bacterial loads in pulmonary granulomas but did not result in disseminated infection.

Frequency of Mtb-specific T cells in granulomas

The magnitude of the Mtb-specific CD4 and CD8 T cell responses was enumerated by intracellular cytokine staining after stimulation with both CD4 and CD8 Mtb peptide megapools (21, 22). Rather than the increased T cell expansion expected to result from PD-1 blockade, we found that the accumulation of Mtb-specific CD4 T cells in the blood and airways was delayed by PD-1 blockade, whereas the kinetics of Mtb-specific CD8 T cell responses in the BAL fluid were similar to control animals (Fig. 3, A and B). The frequency of Mtb-specific CD4 and CD8 T cells in the pulmonary lymph nodes at necropsy was not affected by PD-1 blockade (Fig. 3, C and F). In granulomas, the frequency of Mtb-specific CD4 T cells was similar between isotype control– and α PD-1–treated animals, whereas Mtb-specific CD8 T cells were significantly increased by PD-1 blockade,

although two animals (DG9R and DG2T) did not have elevated CD8 responses (Fig. 3, D and G). These results are in contrast to studies of Mtb infection in PD-1 KO mice, where it was shown that Mtb-specific CD4 T cells in the lungs are significantly increased by PD-1 deficiency and Mtb-specific CD8 T cells were much less affected (10).

PD-1 blockade altered the relationship between the magnitude of the Mtb-specific T cell response and bacterial loads. At bacterial loads lower than ~2000 to 5000 colony-forming units (CFU) per granuloma, there was trend for a positive correlation between Ag-specific T cells and numbers of bacteria, but at higher bacterial loads, this switched to a negative correlation (Fig. 3, E and H). In other words, Ag-specific T cell responses were the highest in granulomas near the middle of the CFU distribution, and the granulomas with the lowest CD4 T cell responses were at either the lowest or highest end of the CFU distribution. We previously observed a nearly identical nonmonotonic relationship between Ag-specific CD4 T cells and bacterial loads in an independent group of macaques that

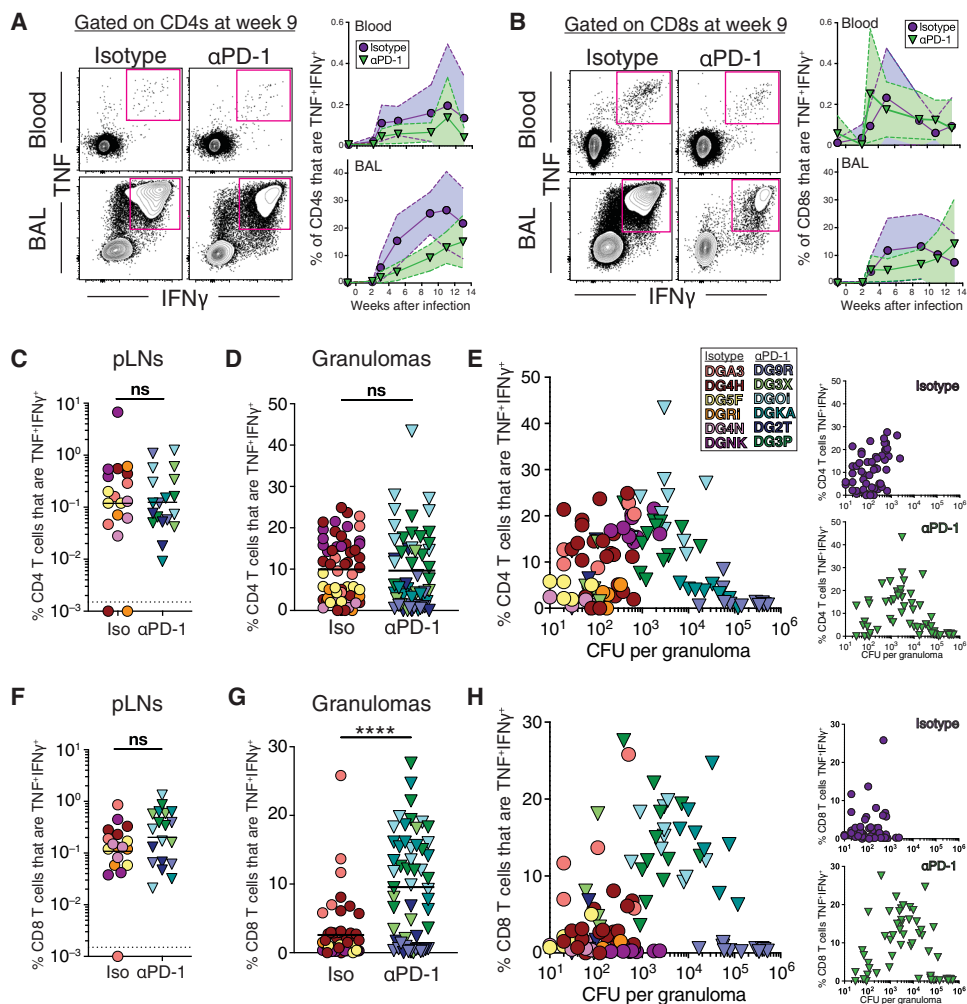


Fig. 3. PD-1 blockade increases Mtb-specific CD8 T cell responses in granulomas. (A) Example fluorescence-activated cell sorting (FACS) plots and summary graphs of CD4 T cells from the blood and BAL after in vitro stimulation with the MTB300 peptide megapool. (B) Example FACS plots and summary graphs of CD8 T cells from the blood and BAL after in vitro stimulation with an Mtb MHC-I peptide megapool. (C and D) Graphs showing the percentage of CD4 T cells in the pulmonary lymph nodes (C) and granulomas (D) that are TNF $^{+}$ IFN γ^{+} after in vitro stimulation. (E) Comparison of the bacterial burden of each granuloma with the percent of CD4 T cells that are TNF $^{+}$ IFN γ^{+} after in vitro stimulation. Small insets display the same information separated by experimental group with isotype control (top) and α PD-1 (bottom). (F and G) Graphs showing the percentage of CD8 T cells in the pulmonary lymph nodes (F) and granulomas (G) that are TNF $^{+}$ IFN γ^{+} after in vitro stimulation. (H) Comparison of the bacterial burden of each granuloma with the percent of CD8 T cells that are TNF $^{+}$ IFN γ^{+} after in vitro stimulation. Small insets display the same information separated by experimental group with isotype control (top) and α PD-1 (bottom). **** $P < 0.0001$.

developed a similarly wide range of granuloma bacterial loads after infection with a more virulent strain of Mtb (23). Therefore, we suggest that this complex relationship between bacterial loads and T cell responses in individual granulomas is not related to PD-1 blockade itself but may be a previously unrecognized normal feature of the heterogeneity in TB granulomas.

PD-1 blockade had no effect on the frequency of Foxp3 $^{+}$ CD4 T cells, MAIT (mucosal associated invariant T) cells, or $\gamma\delta$ T cells in the blood and BAL at any time point after infection or in granulomas at necropsy (fig. S1). Overall, these results show that PD-1 blockade results in increased Mtb-specific CD8 but not CD4 T cell responses in pulmonary lesions at the time of necropsy. We should point out,

however, that we do not know how PD-1 blockade may have affected T cell responses in granulomas at earlier time points.

Function of Mtb-specific T cells in granulomas

We next examined the effect of PD-1 blockade on T cell functionality. Mtb-specific CD4 T cells were identified as TNF $^{+}$ after stimulation with peptide megapools. PD-1 blockade did not change the production of IFN γ , CD153, or granzyme B by Mtb-specific CD4 T cells but resulted in a slight reduction in interleukin-2 (IL-2) and increased IL-17A production (Fig. 4A). Overall, there was very little difference in the functional profile of Mtb-specific CD4 T cells. However, we observed a notable increase in the expression of CTLA (cytotoxic T lymphocyte antigen)-4 on TNF $^{+}$ Mtb-specific CD4 T cells in the granulomas of animals treated with α PD-1 compared with the isotype control mAb (Fig. 4B). This was also observed in infected PD-1 KO mice, where CTLA-4 is up-regulated on Mtb-specific CD4 T cells in the lungs (10). In contrast to CD4 T cells, TNF $^{+}$ Mtb-specific CD8 T cells in granulomas displayed a significant increase in production of IFN γ , IL-2, and granzyme B and did not have elevated CTLA-4 expression (Fig. 4, C and D). Therefore, PD-1 blockade did not increase the number or the functional potential of Mtb-specific CD4 T cells and instead resulted in increased expression of another negative regulatory molecule. In contrast, PD-1 blockade resulted in increases in the number and function of Mtb-specific CD8 T cells. It is important to point out, however, that this analysis measures the potential of the cells to respond to high-level peptide restimulation in vitro, and actual cytokine production may be increased in vivo by PD-1 blockade without

Mtb-specific immunoglobulin G responses

We measured the kinetics of the Mtb-specific immunoglobulin G (IgG) response in isotype control- and α PD-1-treated animals. Antibody responses were low and highly variable between animals, and there was no major difference in the serum Ab levels in control and α PD-1-treated animals at necropsy (fig. S2A). To ask whether Ab responses correlated with bacterial loads, we compared the levels of Mtb-specific IgG with the mean CFU per lung granuloma. There

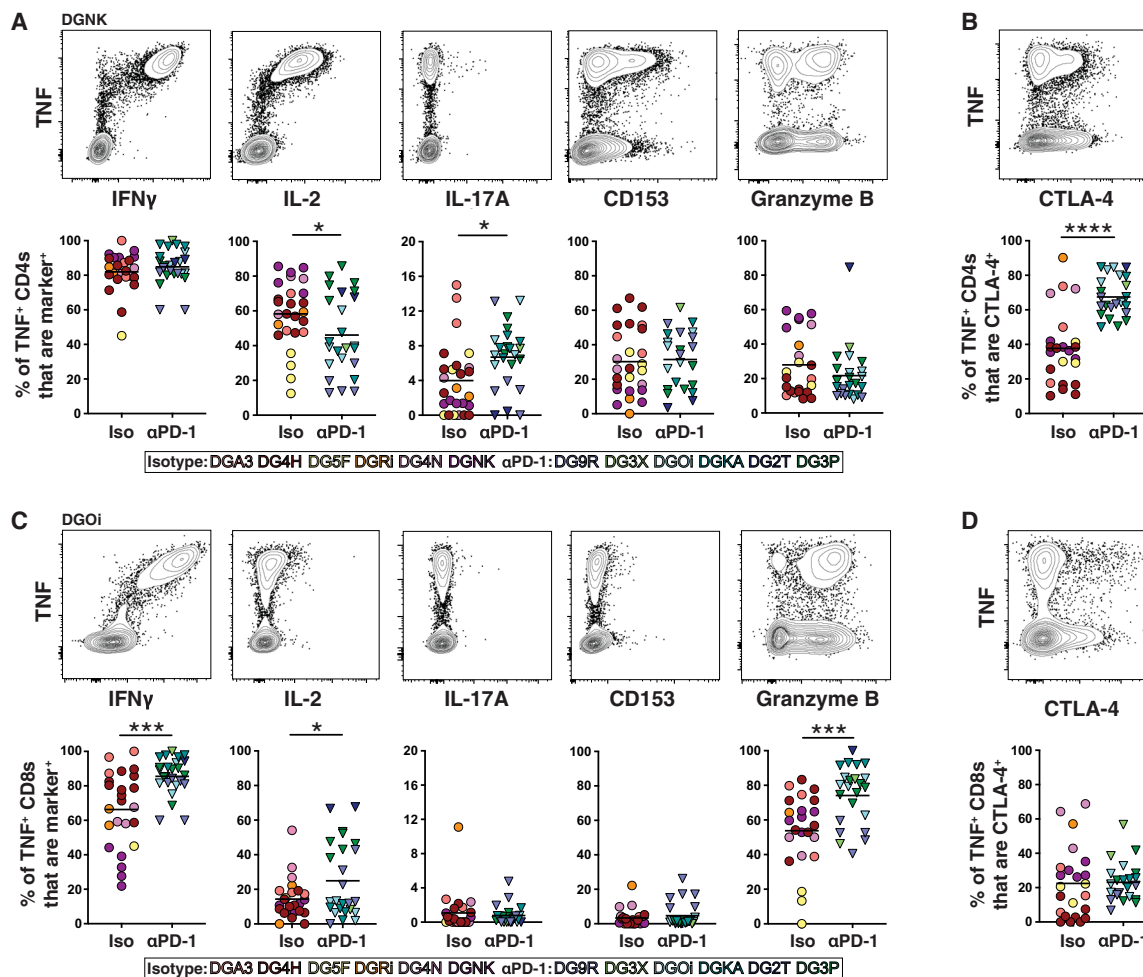


Fig. 4. Enhanced function of Mtb-specific CD8 T cells after PD-1 blockade. (A) Example FACS plots of cytokine staining on total CD4 T cells of a granuloma from animal DGNK and summary graphs of individual cytokines from TNF⁺ CD4 T cells. Each symbol is a granuloma from indicated animal. (B) Example FACS plot of CTLA-4 and TNF staining on total CD4 T cells of a granuloma from animal DGNK and summary graph of percent CTLA-4⁺ of TNF⁺ CD4 T cells. (C) Example FACS plots of cytokine staining on total CD8 T cells of a granuloma from animal DGOI and summary graphs of individual cytokines from TNF⁺ CD8 T cells. Each symbol is a granuloma from indicated animal. (D) Example FACS plot of CTLA-4 and TNF staining on total CD4 T cells of a granuloma from animal DGNK and summary graph of percent CTLA-4⁺ of TNF⁺ CD4 T cells. * $P < 0.05$, *** $P < 0.001$, and **** $P < 0.0001$.

was a strong correlation between the magnitude of the Ab response and bacterial loads in the α PD-1-treated animals [coefficient of determination (R^2) = 0.72, $P = 0.03$] but not the controls ($R^2 = 0.32$, $P = 0.24$) (fig. S2B).

Increased inflammation in granulomas after PD-1 blockade

We first profiled soluble mediators in plasma and granuloma homogenates. Starting ~1 week after the first antibody infusion, there was a large burst of soluble CD40L and CCL3 in plasma of all six α PD-1-treated animals, but these molecules were undetectable in all of the isotype control-treated animals (fig. S3). Moreover, there was a strong correlation between soluble CD40L and CCL3 in the plasma (fig. S3), which may be indicative of systemic T cell activation after PD-1 blockade. We did not perform blockade in uninfected macaques, so it is not clear whether PD-1 blockade would have resulted in systemic CD40L and CCL3 detection in the absence of Mtb infection.

In granulomas, the three cytokines that were the most up-regulated after α PD-1 treatment were IL-18, IFN γ , and TNF (Fig. 5A). This is consistent with mouse model data indicating that IFN γ promotes

pathology in Mtb-infected PD-1^{-/-} mice and with in vitro data showing that TNF can promote increased bacterial growth after PD-1 blockade in an in vitro human 3D granuloma model (11, 12). Sparse canonical correlation analysis (sCCA) showed that the quality of inflammation was greatly affected by PD-1 blockade, with IL-18 a major driver of differences between the two groups (Fig. 5B). Further analysis of the Spearman correlations in the cytokine network found that IFN γ was the largest node of the cytokine network in granulomas isolated from control animals, whereas IL-18 was the most interconnected node in α PD-1-treated animals (Fig. 5C). Overall, we found consistent changes in the correlation matrices, with higher density of network interconnectivity in granulomas from α PD-1 compared with isotype control-treated animals. Increased interconnectivity in cytokine networks has been linked to increased immune activation and augmented inflammatory activity in a wide range of disease settings. The increased cytokine concentrations and interconnectivity between cytokines in networks from α PD-1 macaques collectively indicate that the granulomas from the α PD-1-treated animals presented with increased inflammatory status.

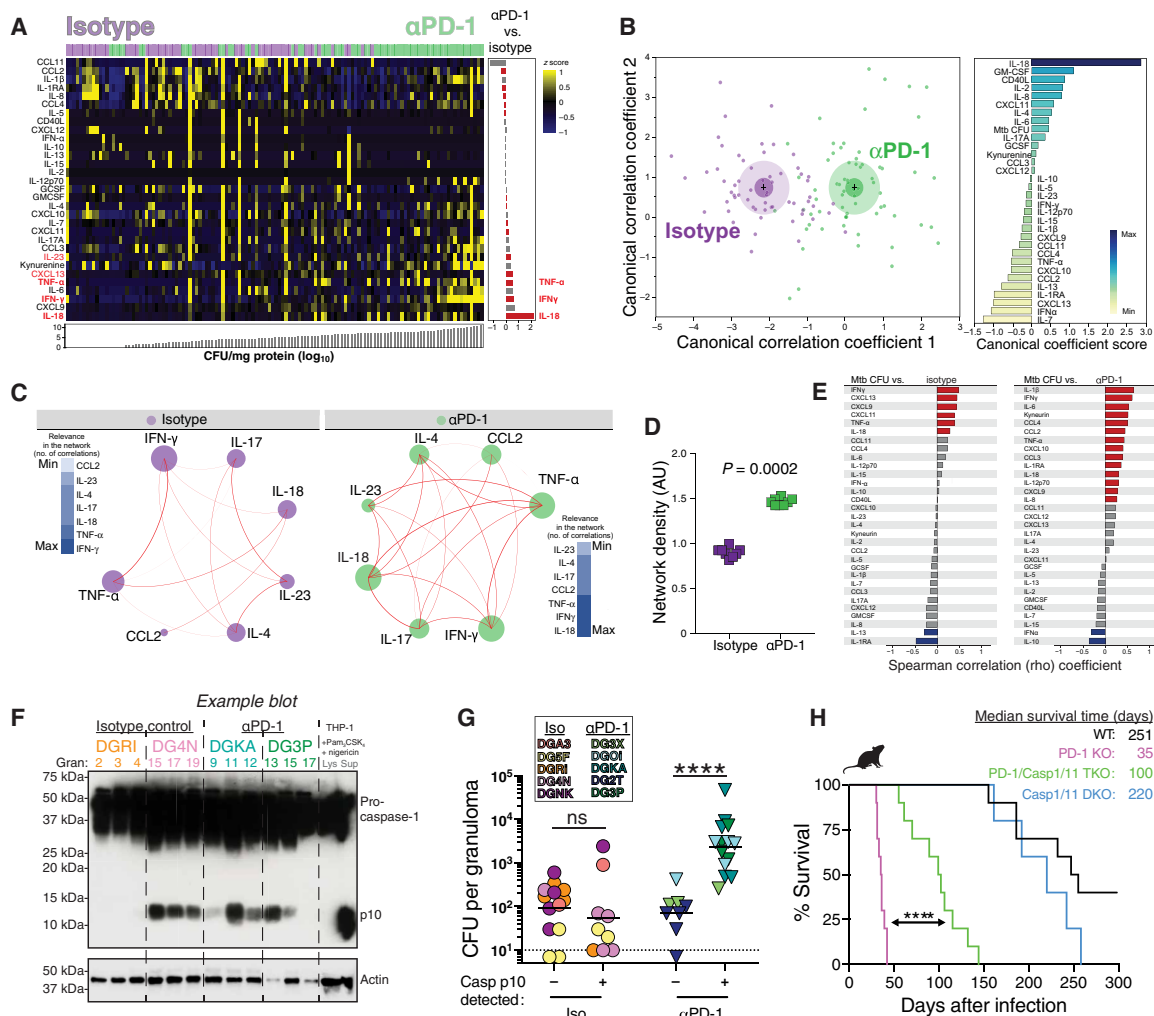


Fig. 5. Increased inflammation in granulomas after PD-1 blockade. Soluble mediators were measured in granuloma homogenate supernatants of isotype control– and α PD-1–treated macaques. Granuloma homogenate samples from DG9R and DG4H were not available and are not included in the cytokine multiplex analysis. (A) Left: Data were log-transformed and z score–normalized. Markers were ranked according to mycobacterial load values (CFU/mg of protein) and fold difference value between the different experimental groups. A heatmap was built to describe the overall expression profile of the inflammatory markers in each granuloma from monkeys labeled according to the experimental group indicated by distinct colors (green for isotype control and purple for α PD-1). Right: Average fold difference values in expression of inflammatory markers in granulomas from monkeys treated with anti-PD1 versus isotype controls are described (log-transformed values). Differences that reached statistical significance with the Mann-Whitney *U* test adjusted for multiple comparisons using the Holm-Bonferroni’s method (adjusted $P < 0.05$) are represented in colored bars. (B) Left: Discrimination of groups using combination of inflammatory biomarkers per granuloma. In an exploratory approach, a sCCA was used to test whether experimental groups could be distinguished on the basis of the overall expression profile of all the markers measured as well as mycobacterial loads (Mtb CFU values per milligram of protein). Right: Canonical coefficient scores were calculated to identify the biomarkers most responsible for the difference between groups in the sCCA model. (C) Spearman correlation matrices of the biomarker expression levels in each study group were built, and Circos plots were used to illustrate the correlation networks. Each circle represents a different plasma parameter. The size of each circle is proportional to the number of significant correlations. The connecting lines represent statistically significant correlations ($P < 0.01$). Red connecting lines represent positive correlations, whereas blue lines infer negative correlations (no negative correlations were found). Color intensity is proportional to the strength of correlation (ρ value). Node analysis was used to illustrate the number of significant correlations per marker. Markers were grouped according to the number of connections from minimum to maximum numbers detected. (D) Network density was compared between the groups using permutation test (100 permutations). AU, arbitrary units. (E) Spearman correlation analysis was used to test association between cytokine values in granulomas and the mycobacterial loads (CFU/mg of protein) in monkeys receiving isotype controls (left) and in those who were treated with α PD-1 (right). Bars represent the Spearman rank (ρ) values. Colored bars indicate statistically significant correlations ($P < 0.05$) after adjustment for multiple measurements. Red color infers positive correlation, whereas blue color denotes negative correlations, and gray bars are nonsignificant associations. (F) Example Western blot of caspase 1 in granuloma homogenates. See fig. S2 for all blots run for this analysis. (G) Bacterial loads in granulomas with detectable active caspase 1 p10 or not in isotype control– or α PD-1–treated macaques. (H) Survival curves and MST (median survival time) of WT, PD-1 KO, caspase 1/11 double-KO (DKO), or PD-1/caspase 1/11 triple-KO (TKO) mice after aerosol Mtb-H37Rv infection. Data are pooled from two independent survival studies. **** $P < 0.0001$.

We next looked for correlations between different soluble mediators and bacterial loads. There were more positive correlations between soluble mediators and bacterial loads in granulomas of α PD-1–

treated animals (14 of 31 analytes) compared with isotype control–treated animals (6 of 31 analytes) (Fig. 5E). Increased levels of IL-18, IFN γ , and TNF positively correlated with bacterial loads in both

experimental groups. Several molecules correlated with CFU only in α PD-1– but not isotype control–treated animals, including IL-1 β ; IL-1RA; IL-6; IL-8; kynurenine; and the chemokines CXCL10, CCL2, CCL3, and CCL4. Of these, IL-1 β had the strongest correlation with bacterial loads in the granulomas of α PD-1–treated animals. Overall, the elevated bacterial loads in the granulomas of the α PD-1–treated animals were associated with increased correlations with inflammatory mediators.

Role of caspase 1 activation in TB exacerbation due to PD-1 blockade

IL-18 was the most differentially expressed cytokine up-regulated in the granulomas of α PD-1–treated animals. Although IL-1 β concentrations were not different between groups, IL-1 β had the strongest positive correlation with bacterial loads in α PD-1–treated animals out of all of the molecules measured. Both of these cytokines are produced as inactive precursors that are processed into bioactive cytokines by caspase 1 inflammasomes, so we next examined caspase 1 activation in granulomas. By Western blot, we found that procaspase 1 was detectable in all granuloma homogenates analyzed but that cleaved caspase 1 was only present in some granulomas (example blot in Fig. 5F and all blots shown in fig. S4). The p10 subunit of caspase 1, a marker of caspase activation, was detected in 11 of 23 granulomas from isotype control–treated animals and 14 of 23 granulomas from α PD-1–treated animals, indicating that the presence of activated inflammasomes was not increased by PD-1 blockade (Fig. 5F and fig. S4). Thus, we did not find evidence of increased caspase 1 inflammasome activation in granulomas after PD-1 blockade.

We next asked whether the presence of activated caspase 1 in granulomas was associated with higher or lower bacterial loads. In isotype control–treated animals, granulomas with detectable p10 had similar bacterial loads compared to granulomas with no detectable p10 subunit (Fig. 5G). In contrast, in α PD-1–treated animals, granulomas with active caspase 1 had significantly elevated bacterial loads. IL-1 β levels trended higher in granulomas containing activated caspase 1 in isotype control–treated animals but were significantly higher in p10⁺ compared with p10⁻ granulomas from α PD-1–treated animals (fig. S5). In contrast, there was no significant difference in IL-18 levels in p10⁺ versus p10⁻ granulomas (fig. S5). Thus, upon PD-1 blockade, caspase 1 activation is not increased but is associated with higher levels of IL-1 β and exacerbation of the infection.

Prompted by the above observations, we next sought to test the possible contribution of inflammatory caspase activation to the exacerbation of Mtb infection during PD-1 blockade using the murine model. As previously shown, PD-1 KO mice succumb rapidly to Mtb infection [(9–11) and Fig. 5H]. However, PD-1/caspase 1/caspase 11 triple-deficient mice lived significantly longer compared with PD-1 KO mice, indicating that caspase 1/11 is directly involved in the early death of PD-1 KO mice. Collectively, these data support previous reports that IFN γ and TNF contribute to increased Mtb bacterial loads during PD-1 blockade and reveal the contribution of caspase 1–driven responses as well.

T cell motility in granulomas

PD-1 has been shown to regulate CD4 T cell motility by regulating T cell receptor (TCR)–induced stop signals upon interaction with Ag-presenting cells (24, 25), so we next examined the impact of PD-1 blockade on T cell positioning and intralymphatic T cell trafficking. First, we examined the partitioning of CD4 T cells into the

infected macrophage-rich core (marked by dense CD11b staining) and the peripheral lymphocyte cuff of the granulomas. We found no difference between the percentages of CD4 T cells localizing to the infected cores of granulomas from isotype control– versus α PD-1–treated macaques (Fig. 6A), suggesting that PD-1/PD-L1 (programmed death ligand-1) interactions may not be a major factor limiting the penetration of CD4 T cells into the region of the granuloma containing the infected macrophages. Although we used mCherry-labeled bacteria in these experiments, the reporter expression plasmid was lost by the time of necropsy and the fluorescence could not be visualized.

We next sought to quantify the motility of CD4 T cells in macaque tuberculomas. To do so, we performed live imaging of thick section explants of freshly isolated granulomas (fig. S6A and movie S1). To identify high-quality tracks, we excluded tracks composed of less than five individual spots, tracks that were on the top or bottom of the Z-stack, tracks whose displacement was limited by the top or bottom of the slice, and tracks that displayed significant costaining for non-T cell markers such as CD20 or CD11b (fig. S6B). We found a high degree of heterogeneity in the movement of CD4 T cells between granulomas. Some granulomas contained many moving CD4 T cells, whereas others displayed very few, and large differences were seen even in the same macaque (Fig. 6, B and C). We characterized three basic types of T cell motility in granulomas: tracks with low mean velocity and low variation in speed (stopped cells), tracks with high mean speed and low variation in speed (steadily moving cells), and tracks with intermediate mean velocity and high variability (stuttering cells) (Fig. 6, D and E). We specifically focused on the steadily moving CD4 T cells. Collectively, there was a significant, albeit small, trend for there to be fewer granulomas with an abundance of steadily moving cells in the α PD-1–treated animals (Fig. 6F). The mean velocity of cells that were steadily moving, however, was not different in granulomas from isotype control– and α PD-1–treated macaques (Fig. 6G). Therefore, PD-1 blockade did not affect the speed of cells that were moving, but it resulted in a reduction in the frequency of granulomas that had abundant motile CD4 T cells.

Association between TB exacerbation after PD-1 blockade and the gut microbiota

The composition of the intestinal microbiota has been shown to influence responsiveness to PD-1 blockade during cancer immunotherapy, and in prior work, we noted a correlation between the microbiota composition and disease outcome in Mtb-infected macaques (26–30). In the present study, two animals treated with α PD-1 were nonresponders in that they did not develop increased bacterial loads or disease relative to controls, so we next asked whether exacerbation of TB after PD-1 blockade was associated with the microbiota of the individual macaques. Neither Mtb infection nor PD-1 blockade resulted in changes to the diversity of the intestinal microbiota as measured by the Shannon index (Fig. 7A). However, a trend was observed in which animals with lower granuloma Mtb loads clustered separately from the other animals in their treatment group (DG5F in the isotype control group and DG3X and DG2T in the α PD-1–treated group) (Fig. 7B). The preinfection microbiotas of DG3X and DG2T were similar to each other and significantly different from the “responder” animals (Fig. 7C). Among the α PD-1–treated animals, several bacterial families were specifically enriched in the responder and nonresponder animals (Fig. 7D and fig. S7). Of note, the abundance of Ruminococcaceae has previously been reported to associate with tumor reductions after PD-1 blockade

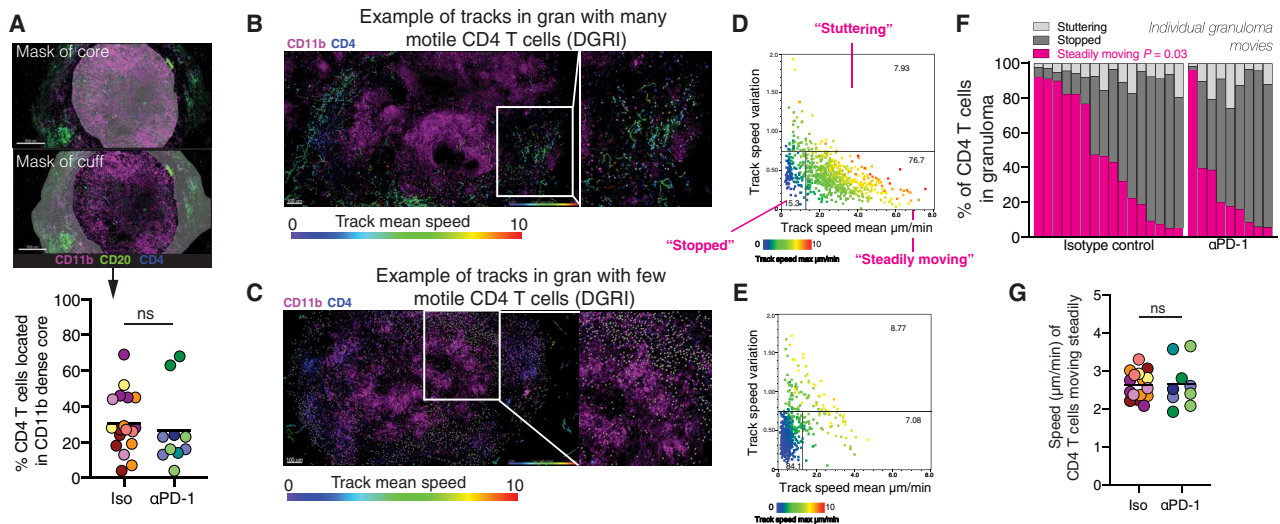


Fig. 6. PD-1 blockade reduces CD4 T cell trafficking in granulomas. (A) Example image of masking to delineate granuloma core and cuff and summary graph of percent of CD4 T cells that localized in the granuloma core. (B and C) Granuloma explants were stained and imaged live to monitor T cell trafficking. Example images show CD4 T cell tracks from granulomas with (B) many motile and (C) few motile cells superimposed on the overall granuloma structure. Both example granulomas are from animal DGRI (isotype control). (D and E) Plotting the mean speed and track speed variation of CD4 T cell tracks shown in the granulomas to the left identifies three basic types of movement: (i) low mean and variation in speed tracks (stopped), (ii) tracks with high mean speed and low speed variation are designated (steadily moving), and (iii) tracks with intermediate mean speed and high variation were designated (stuttering). Panel (D) corresponds to the image of the highly motile granuloma in (B) and panel (E) corresponds to the granuloma in (C) with very few motile CD4 T cells. (F) Percent of each CD4 T cell movement type in each granuloma movie. Each bar represents an individual granuloma from either isotype control- or α PD-1-treated animals. Pink bar indicates the percent of CD4 T cells that were found to be steadily moving during the movie capture. (G) Average speed (micrometers per minute) of CD4 T cells. Each dot represents the average of all “steadily moving” CD4 T cells in an individual granuloma movie. All analysis was performed at a predetermined necropsy done during weeks 15 and 16.

(29), and here, this family was strongly enriched in the monkeys that developed increased Mtb burdens after PD-1 blockade. Therefore, similar to its influence on antitumor responses after PD-1 blockade given for cancer immunotherapy, the intestinal microbiota may also have a role in determining the outcome of PD-1 blockade during Mtb infection.

DISCUSSION

These data indicate that negative regulation of immune responses is a critical aspect of host resistance to Mtb infection. The mechanisms underlying the increased Mtb bacterial loads after PD-1 blockade in infected macaques are not clear. IFN γ and TNF have both been previously implicated in increased growth of Mtb after PD-1 blockade (11, 12). Here, IFN γ , TNF, and IL-18 were the most dysregulated cytokines in granulomas, and each positively correlated with bacterial loads after PD-1 blockade. In vitro studies have shown that stimulating Mtb-infected macrophages with high concentrations of IFN γ leads to the death of the macrophage instead of the expected killing of the bacteria (31, 32), consistent with our hypothesis that T helper 1 cell function needs to be appropriately balanced for optimal control of the infection. We have now shown that caspase 1 activation is also required for exacerbation of Mtb infection after PD-1 blockade. We did not find evidence that PD-1 blockade increased caspase 1 activation in infected macaques, but only granulomas with activated caspase 1 displayed increased bacterial loads after PD-1 blockade. This raises the interesting possibility that PD-1 blockade resulted in the preferential exacerbation of Mtb infection only in the subset of granulomas with ongoing caspase 1 activation. It is not clear whether the detrimental effects of caspase 1 during

PD-1 blockade are due to its role in generating inflammatory cytokines or mediating pyroptotic cell death. It is also not clear why the cleaved p10 subunit of caspase 1 was only detected in a subset of granulomas in the first place. However, our findings clearly demonstrate that inflammatory pathways, normally important for host defense, are required for the exacerbation of Mtb infection after PD-1 blockade.

In mice, we have previously shown that both CD4 and CD8 T cells contributed to the early death of Mtb-infected PD-1 KO mice (10), with CD4 T cells playing a more prominent role. Although we cannot draw conclusions regarding the contributions of CD4 and CD8 T cells to the detrimental outcome of PD-1 blockade in the present macaque study, there was a notable difference in the effect of PD-1 blockade on these two T cell subsets. The expansion and function of Mtb-specific CD8 T cells in granulomas were significantly enhanced after PD-1 blockade, whereas Mtb-specific CD4 T cells displayed no apparent increase in number and function. Instead, Ag-specific CD4 T cell accumulation in the airways was delayed, and the cells expressed high levels of CTLA-4 and displayed reduced motility in granulomas. These observations suggest that disrupting PD-1-dependent regulation may have negative consequences on some CD4 T cell functions. PD-1 primarily regulates signals through the TCR and CD28 (33–35), which are arguably the principal molecules that T cells use to sense their environment and decide how to respond. Therefore, alterations in normal PD-1-mediated modulation of signals 1+2 should be expected to affect many aspects of T cell behavior in vivo, perhaps in unexpected ways. Counterintuitively, it is possible that coinhibition may be required for optimal protection against TB not only by preventing the detrimental overproduction of inflammatory products such as IFN γ and TNF but also because PD-1-mediated tuning of TCR and CD28 signaling is important in

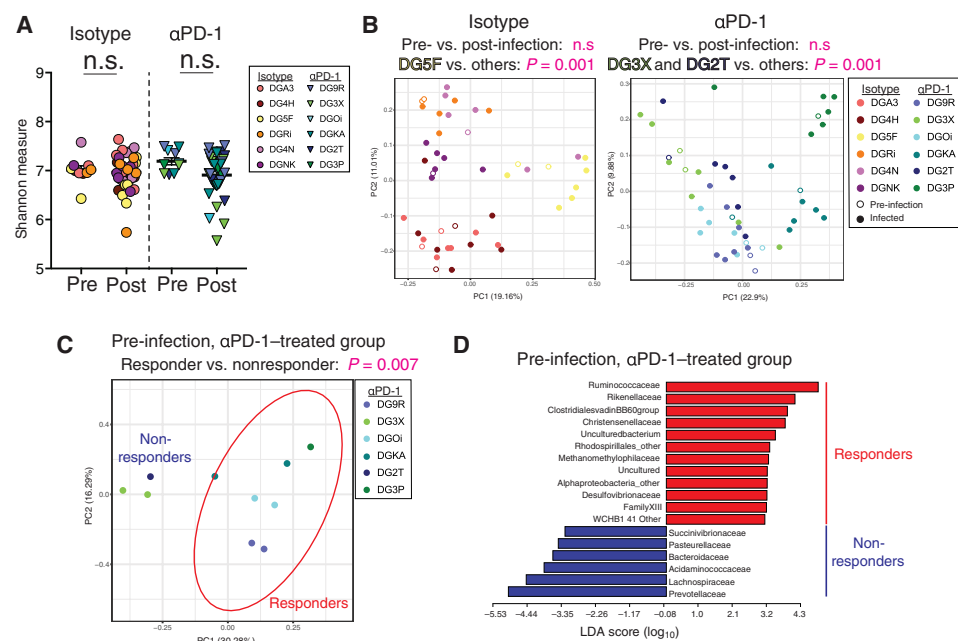


Fig. 7. Exacerbation of Mtb infection by PD-1 blockade is associated with the composition of the preinfection intestinal microbiota of the individual macaque. (A) α diversity for each sample was estimated using the Shannon index. Statistical significance between the pre- and postinfection time points within the isotype or α PD-1 group was calculated using Mann-Whitney U test. (B) β -diversity analyses were performed using the Bray-Curtis dissimilarity matrix for each group and represented on a principal component (PC) plot. Each circle denotes a time point and is colored by monkey as indicated in the key with open and closed circles representing pre- and postinfection time points, respectively. Statistical significance was calculated using permutational multivariate analysis of variance with 999 permutations between pre- and postinfection time points and animals as indicated for both study groups. DG5F in the isotype group and DG3X and DG2T in the α PD-1 group were monkeys with mild TB disease within that group and were compared to animals with severe TB in the same group. (C) β -diversity analysis of just the preinfection sample sequence data from the α PD-1 group is represented on a PC plot. Statistical significance was calculated between animals that progressed to mild (nonresponder) versus severe (responder) TB disease as previously specified. (D) LefSe was used to identify differentially abundant bacterial families in the preinfection microbiota of the nonresponder versus responder monkeys in the α PD-1 group. LDA, local density approximation.

allowing other normally beneficial T cell functions during chronic infection. These two possibilities are not mutually exclusive. It is also important to note that the changes in T cell function observed after PD-1 blockade are likely a combination of the direct effects of the loss of PD-1 signaling and the secondary effects of higher bacterial loads after PD-1 blockade, and it is not possible to quantify the relative contributions of these two factors in macaque studies.

The timing of blockade relative to infection and the particular pathogen present are likely key factors in determining whether PD-1 blockade will be beneficial versus detrimental in any given infectious setting. For example, during chronic lymphocytic choriomeningitis virus infection in mice, PD-1 blockade several months after infection results in enhanced CD8 T cell responses and reductions in viral loads, whereas blockade in the first week of infection results in the rapid death of the animal due to CD8 T cell-mediated destruction of vascular endothelium (36). Here, we started PD-1 blockade at the approximate time of T cell priming after Mtb infection, and it is not clear whether PD-1 blockade will exacerbate TB when initiated at late stages of infection. PD-1 blockade is unlikely to exacerbate all mycobacterial infections, because among different mycobacterial species, the impact of PD-1 deficiency on infection outcome varies. For example, PD-1-deficient mice succumb after Mtb infection but clear BCG infection more rapidly than WT controls (9–11, 37).

Although the data indicate that PD-1 blockade is not likely to be a tenable HDT for TB, this is not the case for all infections. For example, PD-1 blockade has been shown to enhance resistance to several viral (38–40), bacterial (41), parasitic (42), and fungal (43, 44) infections in mice, simian immunodeficiency virus in macaques (45, 46), and JC virus in progressive multifocal leukoencephalopathy in humans (47).

These data highlight the potential challenge of enhancing inflammatory responses as an HDT strategy for TB. The possibility of disease exacerbation seems a major concern for approaches meant to boost host responses during Mtb infection. However, there may be safe ways to stimulate protective host responses against Mtb infection by modulating other immune checkpoint molecules. For example, mice deficient in another co-inhibitory receptor, TIM-3 (T-cell immunoglobulin and mucin domain-3), are more resistant to Mtb infection (48). A better understanding of the role of different checkpoint molecules in the regulation of host responses in TB will aid in the development of HDTs for TB.

With our findings in macaques confirming the murine model data and accumulating clinical case reports, it seems prudent that TB should be considered a potential serious adverse event of PD-1-targeting therapies. The relative risk of TB after PD-1 blockade is not clear, but in this study, four of six macaques developed increased bacterial loads after PD-1 blockade (even during infection with a less virulent strain), indicating that checkpoint blockade-associated exacerbation of TB might not be rare in Mtb-infected individuals. As has been demonstrated during PD-1-targeting cancer therapies, the outcome of Mtb infection during PD-1 blockade also may be influenced by other host factors such as the composition of the intestinal microbiome. On the basis of the combined clinical and experimental data, it seems warranted that patients should be tested for Mtb exposure before initiation of PD-1-targeting immunotherapy and then monitored for development of active TB during treatment. It is also increasingly clear that TB is an important concern in the development of novel immune checkpoint-targeting cancer immunotherapies, as is already the case for immunosuppressive drugs like TNF and Janus kinase inhibitors. As additional co-inhibitory receptors are evaluated as targets for cancer immunotherapy, it will be important to address the possibility of TB as an adverse event.

MATERIALS AND METHODS

Rhesus macaques

Twelve healthy, male, 2-year-old rhesus macaques were received from the National Institute of Allergy and Infectious Diseases (NIAID)

breeding colony on Morgan Island, South Carolina and were tuberculin skin test negative. Animals were housed in nonhuman primate biocontainment racks and maintained in accordance with the Animal Welfare Act; the Guide for the Care and Use of Laboratory Animals; and all applicable regulations, standards, and policies in a fully Association for Assessment and Accreditation of Laboratory Animal Care (AAALAC) International-accredited Animal Biosafety Level 3 (ABSL3) vivarium. All procedures were performed using appropriate anesthetics as listed in the NIAID DIR (Division of Intramural Research) Animal Care and Use Committee-approved animal study proposal LPD 25E. Euthanasia methods were consistent with the AVMA (American Veterinary Medical Association) Guidelines on Euthanasia and end point criteria listed in the NIAID DIR Animal Care and Use Committee-approved animal study proposal LPD 25E.

Rhesus macaque infections and in vivo antibody blockade

Animals were infected with 30 to 50 CFU of an mCherry-expressing H37Rv strain of Mtb. For infection, animals were anesthetized and 2 ml of saline containing the bacteria was bronchoscopically instilled into the right lower lung lobe. Infection dose was confirmed by plating of aliquots onto 7H11 agar plates. At weeks 2, 4, 6, 8, 10, and 13 after infection, animals were intravenously infused with 10 mg/kg of body weight of either rhesus macaque IgG4 isotype control antibody (DSPR4) obtained from the NHP Reagent Resource or α PD-1 (humanized clone EH12 κ variable domains with rhesus macaque κ and IgG4 constant regions) (49, 50).

Mouse infections

C57BL/6 mice were purchased from Taconic Farms (Germantown, NY). PD-1 KO and caspase 1/11 double-KO mice were obtained through a supply contract between the NIAID/National Institutes of Health (NIH) and Taconic Farms. PD-1 KO mice were crossed to caspase 1/11 double-KO mice in an NIAID animal facility. All animals (8 to 12 weeks old, sex matched) were housed in an AAALAC International-accredited ABSL3 NIAID facility in accordance with the National Research Council Guide for the Care and Use of Laboratory Animals. All technical procedures and experimental endpoints were approved by the NIAID Division of Intramural Research Animal Care and Use Committee and listed in the animal study proposal LPD 24E. For Mtb infections, mice were exposed to 100 to 120 CFU of the H37Rv strain of Mtb using an inhalation exposure system (Glas-Col LLC., Terre Haute, IN). Bacterial loads were measured in tissue homogenates by serial dilution on 7H11 agar plates supplemented with oleic acid–albumin–dextrose–catalase (Difco, Detroit, MI).

PET-CT scanning procedures

Rhesus macaques were imaged before infection and every 2 weeks after infection beginning at 4 weeks for a maximum of eight PET-CT scans. Animals were initially anesthetized using glycopyrrolate [0.01 mg/kg intramuscularly (IM)] and a cocktail of ketamine and dexmedetomidine (10 and 0.03 mg/kg, respectively, IM) followed by insertion of an endotracheal tube. The anesthesia plane was maintained with isoflurane (1 to 5% in oxygen) throughout the imaging session. [18 F]FDG doses were determined by measuring the radioactivity content in the syringe using a dose calibrator (Biodex, New York, USA). Blood glucose was measured before injecting [18 F]FDG intravenously (1 mCi/kg). Injected activity and weight of the animal were recorded. During a [18 F]FDG uptake period of 60 min, animals were moved to the bed of an LFER 150 PT/CT scanner

(Mediso Inc., Budapest, Hungary) positioned head first, prone for imaging. While anesthetized, the animal's heart rate, respiration, temperature, peripheral capillary oxygen saturation, and end-tidal CO₂ were monitored. During imaging, animals received 0.9% sodium chloride at 5 to 10 ml/kg/hour intravenously and were mechanically ventilated. A 360-projection CT scan of the lungs was acquired while the animal was maintained in a breath hold for about 50 s. The parameters of the CT scan were as follows: 80 kVp, 0.820 mA, and 80 ms per projection. The resulting CT image was inspected for potential movement or mispositioning and repeated if necessary. The CT data were used to generate a material map for the reconstruction of the corresponding PET image. A 20-min PET dataset was acquired (Coincidence mode 1-9) with the identical field of view during mechanical ventilation. After imaging, animals were administered Antisedan (0.3 mg/kg IM) to reverse sedation and returned to their home cages. The raw CT and PET data were reconstructed (CT: voxel size of 0.5 × 0.5 × 0.5 mm, Butterworth filter; PET: 3D Tera-Tomo reconstruction, eight iterations, nine subsets, voxel size of 0.8 mm with random, attenuation, and scatter correction) using the Nucline software (Mediso Inc., Budapest, Hungary).

PET and CT data analysis

PET and CT DICOM files were coregistered using MIM Maestro (v. 6.2, MIM Software Inc., Cleveland, OH). A lung volume of interest (VOI) was defined on the CT image using methods previously described including adjusting the VOI away from nonlung surfaces by shrinking the VOI by 0.5 mm (51). For CT analysis, a lower threshold of -400 Hounsfield units was applied, and the remaining dense VOI was inspected to confirm the inclusion of only areas of granulomatous disease. For PET analysis, the adjusted CT VOI was transferred to the PET image, and a lower threshold of 2.5 standardized uptake value by body weight was applied to remove background FDG uptake. The remaining FDG uptake in the VOI was considered tubercular disease related (51, 52). Manual removal of nonspecific [18 F]FDG uptake was occasionally required in proximity of large blood vessels and the diaphragm. The software generated tables with all the values recorded for the selected PET and CT volumes for the serial scans. Two readers blind to treatment assignment independently performed the image analysis described above for each animal. If there was more than 5% disagreement, then a third read was included and the disease findings from each assessment were averaged. Three-dimensional projections were generated using Osirix v. 5.9 software (Pixmeo, Geneva, Switzerland).

Cell isolations and stimulations

Blood samples were collected in EDTA tubes, and peripheral blood mononuclear cells were isolated by Ficoll-Paque (GE Life Sciences) density centrifugation. BAL samples were passed through a 100- μ m cell strainer, pelleted, and counted for analysis. Lymph nodes and spleens were dissociated using a gentleMACS Tissue Dissociator (Miltenyi Biotech). Granulomas were individually resected from the lungs, and samples used for flow cytometry analysis were pushed through a 100- μ m cell strainer. Aliquots from all samples were serially diluted and plated on 7H11 agar plates for CFU quantification. Cells were stimulated for 6 hours at 37°C in X-vivo 15 media supplemented with 10% fetal calf serum (FCS) with major histocompatibility complex class I MHC-I and MHC-II (MTB300) Mtb peptide megapools (1 and 2 μ g/ml, respectively) in the presence of brefeldin A and monensin (eBioscience).

Flow cytometry

Fluorochrome-labeled antibodies used for flow cytometric analysis are listed in table S1. Surface Ags and dead cells were stained in phosphate-buffered saline (PBS) + 1% FCS + 0.1% sodium azide for 30 min at 4°C. For intracellular cytokine and transcription factor staining, cells were fixed and permeabilized with the Foxp3 Transcription Factor Staining Buffer Kit (eBioscience) and stained for 30 min at 4°C. Samples were acquired on a FACSymphony (BD Biosciences), and data were analyzed using FlowJo 10 (Tree Star). Lymphocytes were gated on by the exclusion of dead cells and doublets and were CD3⁺. The gating strategies used for specific T cell subsets are shown in fig. S8.

Measurement of Mtb-specific IgG

Half-area 96-well enzyme-linked immunosorbent assay (ELISA) plates (Corning no. 3690) were coated with 25 µl of Mtb whole-cell lysate (strain H37Rv, BEI Resources) at 10 µg/ml diluted in PBS for 1 hour at 37°C. The plates were washed using AquaMax 2000 (Molecular Devices) three times with 100 µl of PBST (PBS plus 0.05% Tween 20) wash buffer. Plates were blocked overnight at 4°C in 50 µl of block buffer (5% milk powder + 4% whey buffer in PBS Tween 20). Plates were then washed, and plasma samples were added at serial 1:3 dilutions starting at a 1:10 dilution with 4% whey buffer and incubated for 1 hour at 37°C. After washing, plates were incubated with detection antibody; 25 µl of goat anti-monkey IgG (H+L)-horseradish peroxidase (HRP) (catalog no. NB7215, Novus Biologicals) was added at 1:1000 dilution in 4% whey buffer for 1 hour at 37°C. A wash was performed and 25 µl of 1-Step Ultra TMB-ELISA Substrate Solution (Thermo Fisher Scientific no. 34029) was added to develop the plates. The reaction was stopped by adding 50 µl of 0.5 M sulfuric acid, and the optical density was measured at 450 nm. The area under the curve of log-transformed values was determined in GraphPad Prism, and the preinfection baseline was subtracted from each postinfection time point sample to calculate Mtb-specific IgG.

Multiplex cytokine analysis

Granuloma homogenates and plasma samples were sterile-filtered and analyzed for protein concentrations using the Invitrogen Cytokine and Chemokine 30-Plex ProcartaPlex kit (Thermo Fisher Scientific). Samples were acquired on a MAGPIX with xPONENT software (Luminex Corporation). A kynurenine ELISA was also performed using assay instructions on the homogenate samples (Labor Diagnostika Nord). Statistical analysis of this data is described below.

Western immunoblotting

Total protein from granuloma supernatants was normalized by dilution in 1× tris-buffered saline (TBS). THP-1 monocytes were plated in Opti-MEM (Gibco) + 1% FCS and treated with Pam₃CSK₄ (500 ng/ml; InvivoGen) for 4 hours and 10 µM nigericin (InvivoGen) for an additional 1 hour. A total of 1.2 × 10⁶ cells were lysed in 300-µl radioimmunoprecipitation assay buffer supplemented with cOmplete Protease Inhibitor Cocktail (Roche) on ice for 30 min and passed through 30-µm polyethylene filter spin columns (Pierce) to shred genomic DNA. Two milliliters of cell-free THP-1 supernatant was concentrated to 100 µl by methanol-chloroform precipitation (53). All samples were denatured by addition of SDS sample buffer (final concentration, 70 mM SDS) and boiling for 5 min. Eight nanograms of granuloma protein was loaded per lane into Any kD Mini-PROTEAN TGX gels

(Bio-Rad), separated by SDS-polyacrylamide gel electrophoresis and transferred to 0.2-µm nitrocellulose membranes (Bio-Rad). Transfer and loading were validated by staining membranes in 0.2% Ponceau S solution (Sigma-Aldrich) for 2 min. Membranes were blocked in 5% skim milk in TBS + 0.1% Tween 20 (TBS-T) for 1 hour at room temperature before incubation in primary antibody overnight at 4°C (rabbit-α-caspase 1, Abcam no. ab179515, 1:1000). Membranes were washed in TBS-T, incubated in secondary antibody for 1 hour at room temperature (donkey-α-rabbit-HRP, Jackson ImmunoResearch no. 711-035-152, 1:10,000; mouse-α-actin-HRP, Santa Cruz Biotechnology no. sc-47778, 1:10,000), washed, and coated in Immobilon Western Chemiluminescent HRP Substrate (Millipore). Immunoreactivity was imaged using either Amersham Hyperfilm ECL (GE Healthcare) and an X-OMAT 2000A processor (Kodak) (for caspase 1) or a ChemiDoc Touch Imaging System (Bio-Rad) (for actin).

Confocal imaging and analysis

Granulomas were embedded in RPMI containing 2% agarose and sliced into 300- to 350-µm sections using Leica VT1000 S Vibrating Blade Microtome (Leica Microsystems, Exton, PA). Tissue sections were stained with fluorescently labeled antibodies specific for CD4, CD8, CD11b, CD20, or PD-1 (eBioscience) for 2 hours on ice. After staining sections were washed three times and cultured in complete lymphocyte medium (phenol red-free RPMI supplemented with 10% fetal bovine serum, 10% rhesus plasma, 25 mM Hepes, 2 mM L-glutamine, 1% sodium pyruvate, and 1% penicillin and streptomycin) in a humidified incubator at 37°C. Sections were imaged using a Leica SP5 inverted five-channel confocal microscope equipped with an Environmental Chamber (NIH Division of Scientific Equipment and Instrumentation Services) to maintain 37°C and 5% CO₂. Microscope configuration was set up for 4D analysis (*x*, *y*, *z*, and *t*) of cell segregation and migration within tissue sections. Diode laser for 405-nm excitation, argon laser for 488-nm excitation, diode-pumped solid-state laser for 561-nm excitation, and HeNe lasers for 594- and 633-nm excitation wavelengths were tuned to minimal power (between 1 and 5%). Mosaic images of complete granuloma sections were generated by acquiring each *xy* plane with 10 to 50-µm *z* spacing every 10 s for 3 to 4 hours using motorized stage to cover the whole section area and assembled into a tiled image using LAS X software (Leica Microsystems, Exton, PA). Motion artifacts, 3D alignment, and thermal drift of sequential *z* sections was corrected using cross-correlation algorithm in Huygens Pro software package (version 20.04.0p2, Scientific Volume Imaging BV, Hilversum, The Netherlands). Postacquisition images were processed using Imaris software (version 9.5.1, Bitplane AG, Zurich, Switzerland) for quantification and visualization. Localizations of the cells in granulomas were identified on the basis of fluorescence intensity using spot function of Imaris and divided into different regions based on localization using surface 3D reconstruction and channel masking method. Multiparameter track data generated by the Imaris analysis of granuloma movies were imported in FlowJo to facilitate visualization and exploration of the data. Data gated in FlowJo were reimported into Imaris using custom-generated Python script for spatial analysis to further localize and visualize cell subpopulations.

Microbiota analyses

Fecal samples were collected from the study animals at two time points in the month before infection and at weeks 2, 3 (only for DG3X,

DG9R, DG4H, and DGA3), 5, 7, 9, 11, and 13 after infection and frozen at -80°C . The week 13 postinfection time point was not collected from monkey DGOi. At the end of the experimental timeline, DNA was extracted from 0.04 to 0.05 g of stored fecal material using QIAamp Fast DNA stool Mini kit (Qiagen, Hilden, Germany) as previously described (54). The V4 region of the 16S RNA gene was amplified with primers 5'-TCGTCGGCAGCGTCAGATGTG-TATAAGAGACAGGTGCCAGCMGCCGCGGTAA-3' and 5'-GTCTCGTGGGCTCGGAGATGTGTATAAGAGACAGG-GACTACHVGGGTWTCTAAT-3' and sequenced on an Illumina MiSeq Platform as previously described (54). The raw fastq data were demultiplexed, and the reads were processed, denoised, and filtered for chimeras using the DADA2 algorithm implemented in QIIME2 version 2-2018.4 (55) resulting in an average of 64,134 reads per sample. Taxonomic classification was performed using Silva database release 132 (56). The week 7 time point from monkey DGRi was dropped from further analysis because this sample sequenced poorly. α and β -diversity analyses on read data rarefied to a depth of 44,000 reads were performed using the Shannon and Bray-Curtis dissimilarity indices, respectively. Linear discriminant analysis (LEfSe) was used to identify differentially abundant taxa between the groups compared, and taxa with a linear discriminant score of >2 and $P < 0.05$ were considered significantly different (57).

Statistical analysis

Biomarker levels were \log_{10} -transformed and normalized by milligrams of protein. Limit of detection values were subtracted. Data were compared between the study groups using the Mann-Whitney U test (two-group comparisons) to identify the biomarkers that were statistically significant between groups. P values were adjusted for multiple measurements using Holm-Bonferroni's method when appropriate. Hierarchical cluster analyses (Ward's method), with $100\times$ bootstrap of z score-normalized data were used to depict the overall expression profile of indicated biomarkers in the study groups.

sCCA modeling was used to assess whether combinations of soluble mediators could discriminate between isotype control and α PD-1 groups (R script: www.jstatsoft.org/article/view/v023i12). The sCCA algorithm was chosen because many variables were studied, and it allows for us to test whether experimental groups could be distinguished on the basis of the overall expression profile of all the markers measured as well as mycobacterial loads (Mtb CFU values per milligram of protein). This approach reduces dimensionality for two codependent datasets (biomarker profile and PD-1 blockade) simultaneously so that the discrimination of the clinical end points represents a combination of variables that are maximally correlated. Thus, trends of correlations between parameters in different clinical groups rather than their respective distribution within each group are the key components driving the discrimination outcome. In our CCA model, simplified and adapted from previously reported investigations of biomarkers for TB diagnosis (58, 59), linear regression graphs represent coefficients from different combinations of plasma factors and baseline characteristics. In the biomarker profile dataset, we included values of all the inflammatory marker variables. Correlations were examined using the Spearman rank test. In the network analysis based on Spearman correlations, nodes represent each given marker and lines represent statistically significant correlations [correlation coefficient (ρ) $> \pm 0.5$ and $P < 0.05$]. The statistical analyses were performed using JMP 14 (SAS, Cary, NC) and

Prism 7.0 (GraphPad Software, San Diego, CA) and R statistical software.

SUPPLEMENTARY MATERIALS

immunology.sciencemag.org/cgi/content/full/6/55/eabf3861/DC1

Fig. S1. Impact of PD-1 blockade on regulatory T cells, MAIT cells, and $\gamma\delta$ T cell frequencies in Mtb-infected macaques.

Fig. S2. Mtb-specific IgG responses.

Fig. S3. PD-1 blockade increases plasma levels of CD40L and CCL3.

Fig. S4. Detection of activated caspase 1 in granuloma homogenates.

Fig. S5. Association of IL-1 β and IL-18 levels with caspase 1 activation in granulomas.

Fig. S6. Live imaging of macaque pulmonary granulomas.

Fig. S7. Correlation between preinfection intestinal microbiota abundance and lung mycobacterial load at necropsy.

Fig. S8. Flow cytometry gating strategy.

Table S1. List of flow cytometry panels used in this study.

Table S2. Raw data file (Excel spreadsheet).

Movie S1. Example live imaging movie of thick-section granuloma explant.

[View/request a protocol for this paper from Bio-protocol.](#)

REFERENCES AND NOTES

1. WHO, Global Tuberculosis Report 2019 (2019); www.who.int/tb/publications/global_report/en/.
2. S. H. E. Kaufmann, A. Dorhoi, R. S. Hotchkiss, R. Bartschlagler, Host-directed therapies for bacterial and viral infections. *Nat. Rev. Drug Discov.* **17**, 35–56 (2018).
3. R. S. Wallis, R. Hafner, Advancing host-directed therapy for tuberculosis. *Nat. Rev. Immunol.* **15**, 255–263 (2015).
4. S. Tiberi, N. du Plessis, G. Walzl, M. J. Vjecha, M. Rao, F. Ntouni, S. Mfinanga, N. Kapata, P. Mwaba, T. D. McHugh, G. Ippolito, G. B. Migliori, M. J. Maeurer, A. Zumla, Tuberculosis: Progress and advances in development of new drugs, treatment regimens, and host-directed therapies. *Lancet Infect. Dis.* **18**, e183–e198 (2018).
5. M. N. Wykes, S. R. Lewin, Immune checkpoint blockade in infectious diseases. *Nat. Rev. Immunol.* **18**, 91–104 (2018).
6. A. Ribas, J. D. Wolchok, Cancer immunotherapy using checkpoint blockade. *Science* **359**, 1350–1355 (2018).
7. M. Rao, D. Valentini, E. Dodoo, A. Zumla, M. Maeurer, Anti-PD-1/PD-L1 therapy for infectious diseases: Learning from the cancer paradigm. *Int. J. Infect. Dis.* **56**, 221–228 (2017).
8. C. L. Day, D. A. Abrahams, R. Bunjun, L. Stone, M. de Kock, G. Walzl, R. J. Wilkinson, W. A. Burgers, W. A. Hanekom, PD-1 expression on *Mycobacterium tuberculosis*-specific CD4 T cells is associated with bacterial load in human tuberculosis. *Front. Immunol.* **9**, 1995 (2018).
9. E. Lazar-Molnar, B. Chen, K. A. Sweeney, E. J. Wang, W. Liu, J. Lin, S. A. Porcelli, S. C. Almo, S. G. Nathenson, W. R. Jacobs, Programmed death-1 (PD-1)-deficient mice are extraordinarily sensitive to tuberculosis. *Proc. Natl. Acad. Sci. U.S.A.* **107**, 13402–13407 (2010).
10. D. L. Barber, K. D. Mayer-Barber, C. G. Feng, A. H. Sharpe, A. Sher, CD4 T cells promote rather than control tuberculosis in the absence of PD-1-mediated inhibition. *J. Immunol.* **186**, 1598–1607 (2011).
11. S. Sakai, K. D. Kauffman, M. A. Sallin, A. H. Sharpe, H. A. Young, V. V. Ganusov, D. L. Barber, CD4 T cell-derived IFN- γ plays a minimal role in control of pulmonary *Mycobacterium tuberculosis* infection and must be actively repressed by PD-1 to prevent lethal disease. *PLOS Pathog.* **12**, e1005667 (2016).
12. L. B. Tezera, M. K. Bielecka, P. Ogongo, N. F. Walker, M. Ellis, D. J. Garay-Baquero, K. Thomas, M. T. Reichmann, D. A. Johnston, K. A. Wilkinson, M. Ahmed, S. Jogai, S. N. Jayasinghe, R. J. Wilkinson, S. Mansour, G. J. Thomas, C. H. Ottensmeier, A. Leslie, P. T. Elkington, Anti-PD-1 immunotherapy leads to tuberculosis reactivation via dysregulation of TNF- α . *eLife* **9**, (2020).
13. D. L. Barber, S. Sakai, R. R. Kudchadkar, S. P. Fling, T. A. Day, J. A. Vergara, D. Ashkin, J. H. Cheng, L. M. Lundgren, V. N. Raabe, C. S. Kraft, J. J. Nieva, M. A. Cheever, P. T. Nghiem, E. Sharon, Tuberculosis following PD-1 blockade for cancer immunotherapy. *Sci. Transl. Med.* **11**, eaat2702 (2019).
14. K. Fujita, T. Terashima, T. Mio, Anti-PD1 antibody treatment and the development of acute pulmonary tuberculosis. *J. Thorac. Oncol.* **11**, 2238–2240 (2016).
15. J. J. Lee, A. Chan, T. Tang, Tuberculosis reactivation in a patient receiving anti-programmed death-1 (PD-1) inhibitor for relapsed Hodgkin's lymphoma. *Acta Oncol.* **55**, 519–520 (2016).
16. Y. C. Chu, K. C. Fang, H. C. Chen, Y. C. Yeh, C. E. Tseng, T. Y. Chou, C. L. Lai, Pericardial tamponade caused by a hypersensitivity response to tuberculosis reactivation after anti-PD-1 treatment in a patient with advanced pulmonary adenocarcinoma. *J. Thorac. Oncol.* **12**, e111–e114 (2017).

17. H. Picchi, C. Mateus, C. Chouaid, B. Besse, A. Marabelle, J. M. Michot, S. Champiat, A. L. Voisin, O. Lambotte, Infectious complications associated with the use of immune checkpoint inhibitors in oncology: Reactivation of tuberculosis after anti PD-1 treatment. *Clin. Microbiol. Infect.* **24**, 216–218 (2018).
18. S. Takata, G. Koh, Y. Han, H. Yoshida, T. Shiroyama, H. Takada, K. Masuhiro, S. Nasu, S. Morita, A. Tanaka, S. Hashimoto, K. Uriu, H. Suzuki, Y. Tamura, N. Okamoto, T. Nagai, T. Hirashima, Paradoxical response in a patient with non-small cell lung cancer who received nivolumab followed by anti-*Mycobacterium tuberculosis* agents. *J. Infect. Chemother.* **25**, 54–58 (2019).
19. K. Fujita, Y. Yamamoto, O. Kanai, M. Okamura, K. Nakatani, T. Mio, Development of *Mycobacterium avium* complex lung disease in patients with lung cancer on immune checkpoint inhibitors. *Open Forum Infect. Dis.* **7**, ofaa067 (2020).
20. C. A. Scanga, J. L. Flynn, Modeling tuberculosis in nonhuman primates. *Cold Spring Harb. Perspect. Med.* **4**, a018564 (2014).
21. C. S. Lindestam Arlehamn, D. M. McKinney, C. Carpenter, S. Paul, V. Rozot, E. Makgotlho, Y. Gregg, M. van Rooyen, J. D. Ernst, M. Hatherill, W. A. Hanekom, B. Peters, T. J. Scriba, A. Sette, A quantitative analysis of complexity of human pathogen-specific CD4 T cell responses in healthy *M. tuberculosis* infected South Africans. *PLoS Pathog.* **12**, e1005760 (2016).
22. M. Pomaznoy, R. Kuan, M. Lindvall, J. G. Burel, G. Seumois, P. Vijayanand, R. Taplitz, R. H. Gilman, M. Saito, D. M. Lewinsohn, A. Sette, B. Peters, C. S. Lindestam Arlehamn, Quantitative and qualitative perturbations of CD8⁺ MAITs in healthy *Mycobacterium tuberculosis*-infected individuals. *Immunohorizons* **4**, 292–307 (2020).
23. K. D. Kauffman, M. A. Sallin, S. Sakai, O. Kamenyeva, J. Kabat, D. Weiner, M. Sutphin, D. Schimel, L. Via, C. E. Barry III, T. Wilder-Kofie, I. Moore, R. Moore, D. L. Barber, Defective positioning in granulomas but not lung-homing limits CD4 T-cell interactions with *Mycobacterium tuberculosis*-infected macrophages in rhesus macaques. *Mucosal Immunol.* **11**, 462–473 (2018).
24. B. T. Fife, K. E. Pauken, T. N. Eagar, T. Obu, J. Wu, Q. Tang, M. Azuma, M. F. Krummel, J. A. Bluestone, Interactions between PD-1 and PD-L1 promote tolerance by blocking the TCR-induced stop signal. *Nat. Immunol.* **10**, 1185–1192 (2009).
25. T. Honda, J. G. Egen, T. Lämmermann, W. Kastentmüller, P. Torabi-Parizi, R. N. Germain, Tuning of antigen sensitivity by T cell receptor-dependent negative feedback controls T cell effector function in inflamed tissues. *Immunity* **40**, 235–247 (2014).
26. N. Iida, A. Dzutsev, C. A. Stewart, L. Smith, N. Bouladoux, R. A. Weingarten, D. A. Molina, R. Salcedo, T. Back, S. Cramer, R. M. Dai, H. Kiu, M. Cardone, S. Naik, A. K. Patri, E. Wang, F. M. Marincola, K. M. Frank, Y. Belkaid, G. Trinchieri, R. S. Goldszmid, Commensal bacteria control cancer response to therapy by modulating the tumor microenvironment. *Science* **342**, 967–970 (2013).
27. B. Routy, E. le Chatelier, L. Derosa, C. P. M. Duong, M. T. Alou, R. Daillère, A. Fluckiger, M. Messaoudene, C. Rauber, M. P. Roberti, M. Fidelle, C. Flament, V. Poirier-Colame, P. Popolon, C. Klein, K. Iribarren, L. Mondragón, N. Jacquolot, B. Qu, G. Ferrere, C. Clémenson, L. Mezquita, J. R. Masip, C. Naltet, S. Brosseau, C. Kaderbhai, C. Richard, C. H. Rizvi, F. Leveze, N. Galleron, B. Quinquis, N. Pons, B. Ruffel, V. Minard-Colin, P. Gonin, J. C. Soria, E. Deutsch, Y. Loriot, F. Ghiringhelli, G. Zalcman, F. Goldwasser, B. Escudier, M. D. Hellmann, A. Eggermont, D. Raoult, L. Albiges, G. Kroemer, L. Zitvogel, Gut microbiome influences efficacy of PD-1-based immunotherapy against epithelial tumors. *Science* **359**, 91–97 (2018).
28. V. Matson, J. Fessler, R. Bao, T. Chongsuwat, Y. Zha, M. L. Alegre, J. J. Luke, T. F. Gajewski, The commensal microbiome is associated with anti-PD-1 efficacy in metastatic melanoma patients. *Science* **359**, 104–108 (2018).
29. V. Gopalakrishnan, C. N. Spencer, L. Nezi, A. Reuben, M. C. Andrews, T. V. Karpnits, P. A. Prieto, D. Vicente, K. Hoffman, S. C. Wei, A. P. Cogdill, L. Zhao, C. W. Hudgens, D. S. Hutchinson, T. Manzo, M. Petaccia de Macedo, T. Cotechini, T. Kumar, W. S. Chen, S. M. Reddy, R. Szczepaniak Sloane, J. Galloway-Pena, H. Jiang, P. L. Chen, E. J. Shpall, K. Rezvani, A. M. Alousi, R. F. Chemaly, S. Shelburne, L. M. Vence, P. C. Okhuysen, V. B. Jensen, A. G. Swennes, F. McAllister, E. Marcelo Riquelme Sanchez, Y. Zhang, E. le Chatelier, L. Zitvogel, N. Pons, J. L. Austin-Breneman, L. E. Haydu, E. M. Burton, J. M. Gardner, E. Sirmans, J. Hu, A. J. Lazar, T. Tsujikawa, A. Diab, H. Tawbi, I. C. Glitza, W. J. Hwu, S. P. Patel, S. E. Woodman, R. N. Amaria, M. A. Davies, J. E. Gershenwald, P. Hwu, J. E. Lee, J. Zhang, L. M. Coussens, Z. A. Cooper, P. A. Futreal, C. R. Daniel, N. J. Ajami, J. F. Petrosino, M. T. Tetzlaff, P. Sharma, J. P. Allison, R. R. Jenq, J. A. Wargo, Gut microbiome modulates response to anti-PD-1 immunotherapy in melanoma patients. *Science* **359**, 97–103 (2018).
30. S. Namasivayam, K. D. Kauffman, J. A. McCulloch, W. Yuan, V. Thovarai, L. R. Mittereder, G. Trinchieri, D. L. Barber, A. Sher, Correlation between disease severity and the intestinal microbiome in *Mycobacterium tuberculosis*-infected rhesus macaques. *mBio* **10**, e01018-19 (2019).
31. J. Lee, H. Kornfeld, Interferon-gamma regulates the death of *M. tuberculosis*-infected macrophages. *J. Cell Death* **3**, 1–11 (2010).
32. K. W. Wong, W. R. Jacobs Jr., *Mycobacterium tuberculosis* exploits human interferon γ to stimulate macrophage extracellular trap formation and necrosis. *J. Infect. Dis.* **208**, 109–119 (2013).
33. T. Okazaki, S. Chikuma, Y. Iwai, S. Fagarasan, T. Honjo, A rheostat for immune responses: The unique properties of PD-1 and their advantages for clinical application. *Nat. Immunol.* **14**, 1212–1218 (2013).
34. A. H. Sharpe, K. E. Pauken, The diverse functions of the PD1 inhibitory pathway. *Nat. Rev. Immunol.* **18**, 153–167 (2018).
35. E. Hui, J. Cheung, J. Zhu, X. Su, M. J. Taylor, H. A. Wallweber, D. K. Sasmal, J. Huang, J. M. Kim, I. Mellman, R. D. Vale, T cell costimulatory receptor CD28 is a primary target for PD-1-mediated inhibition. *Science* **355**, 1428–1433 (2017).
36. H. Frebel, V. Nindl, R. A. Schuepbach, T. Braunschweiler, K. Richter, J. Vogel, C. A. Wagner, D. Löffing-Cueni, M. Kurrer, B. Ludewig, A. Oxenius, Programmed death 1 protects from fatal circulatory failure during systemic virus infection of mice. *J. Exp. Med.* **209**, 2485–2499 (2012).
37. S. Sakai, I. Kawamura, T. Okazaki, K. Tsuchiya, R. Uchiyama, M. Mitsuyama, PD-1-PD-L1 pathway impairs T_H1 immune response in the late stage of infection with *Mycobacterium bovis* bacillus Calmette-Guérin. *Int. Immunol.* **22**, 915–925 (2010).
38. D. L. Barber, E. J. Wherry, D. Masopust, B. Zhu, J. P. Allison, A. H. Sharpe, G. J. Freeman, R. Ahmed, Restoring function in exhausted CD8 T cells during chronic viral infection. *Nature* **439**, 682–687 (2006).
39. T. W. Phares, C. Ramakrishna, G. I. Parra, A. Epstein, L. Chen, R. Atkinson, S. A. Stohman, C. C. Bergmann, Target-dependent B7-H1 regulation contributes to clearance of central nervous system infection and dampens morbidity. *J. Immunol.* **182**, 5430–5438 (2009).
40. J. J. Erickson, P. Gilchuk, A. K. Hastings, S. J. Tollefson, M. Johnson, M. B. Downing, K. L. Boyd, J. E. Johnson, A. S. Kim, S. Joyce, J. V. Williams, Viral acute lower respiratory infections impair CD8⁺ T cells through PD-1. *J. Clin. Invest.* **122**, 2967–2982 (2012).
41. S. Yao, S. Wang, Y. Zhu, L. Luo, G. Zhu, S. Flies, H. Xu, W. Ruff, M. Broadwater, I. H. Choi, K. Tamada, L. Chen, PD-1 on dendritic cells impedes innate immunity against bacterial infection. *Blood* **113**, 5811–5818 (2009).
42. J. M. Horne-Debets, D. S. Karunaratne, R. J. Faleiro, C. M. Poh, L. Renia, M. N. Wykes, Mice lacking programmed cell death-1 show a role for CD8⁺ T cells in long-term immunity against blood-stage malaria. *Sci. Rep.* **6**, 26210 (2016).
43. E. Lazar-Molnar, A. Gacser, G. J. Freeman, S. C. Almo, S. G. Nathenson, J. D. Nosanchuk, The PD-1/PD-L costimulatory pathway critically affects host resistance to the pathogenic fungus *Histoplasma capsulatum*. *Proc. Natl. Acad. Sci. U.S.A.* **105**, 2658–2663 (2008).
44. J. A. Rousey, S. P. Viglianti, S. Teitz-Tennenbaum, M. A. Olszewski, J. J. Osterholzer, Anti-PD-1 antibody treatment promotes clearance of persistent cryptococcal lung infection in mice. *J. Immunol.* **199**, 3535–3546 (2017).
45. V. Velu, K. Titanji, B. Zhu, S. Husain, A. Pladevega, L. Lai, T. H. Vanderford, L. Chennareddi, G. Silvestri, G. J. Freeman, R. Ahmed, R. R. Amara, Enhancing SIV-specific immunity in vivo by PD-1 blockade. *Nature* **458**, 206–210 (2009).
46. R. Dyavar Shetty, V. Velu, K. Titanji, S. E. Bosinger, G. J. Freeman, G. Silvestri, R. R. Amara, PD-1 blockade during chronic SIV infection reduces hyperimmune activation and microbial translocation in rhesus macaques. *J. Clin. Invest.* **122**, 1712–1716 (2012).
47. I. Cortese, P. Muranski, Y. Enose-Akahata, S. K. Ha, B. Smith, M. C. Monaco, C. Ryschkewitsch, E. O. Major, J. Ohayon, M. K. Schindler, E. Beck, L. B. Reoma, S. Jacobson, D. S. Reich, A. Nath, Pembrolizumab treatment for progressive multifocal leukoencephalopathy. *N. Engl. J. Med.* **380**, 1597–1605 (2019).
48. P. Jayaraman, M. K. Jacques, C. Zhu, K. M. Steblenko, B. L. Stowell, A. Madi, A. C. Anderson, V. K. Kuchroo, S. M. Behar, TIM3 mediates T cell exhaustion during *Mycobacterium tuberculosis* infection. *PLoS Pathog.* **12**, e1005490 (2016).
49. G. H. Mylvaganam, L. S. Chea, G. K. Tharp, S. Hicks, V. Velu, S. S. Iyer, C. Deleage, J. D. Estes, S. E. Bosinger, G. J. Freeman, R. Ahmed, R. R. Amara, Combination anti-PD-1 and antiretroviral therapy provides therapeutic benefit against SIV. *JCI Insight* **3**, e122940 (2018).
50. D. M. Dorfman, J. A. Brown, A. Shahsafaei, G. J. Freeman, Programmed death-1 (PD-1) is a marker of germinal center-associated T cells and angioimmunoblastic T-cell lymphoma. *Am. J. Surg. Pathol.* **30**, 802–810 (2006).
51. L. E. Via, K. England, D. M. Weiner, D. Schimel, M. D. Zimmerman, E. Dayao, R. Y. Chen, L. E. Dodd, M. Richardson, K. K. Robbins, Y. Cai, D. Hammoud, P. Herscovitch, V. Dartois, J. A. L. Flynn, C. E. Barry III, A sterilizing tuberculosis treatment regimen is associated with faster clearance of bacteria in cavitary lesions in marmosets. *Antimicrob. Agents Chemother.* **59**, 4181–4189 (2015).
52. A. G. White, P. Maiello, M. T. Coleman, J. A. Tomko, L. J. Frye, C. A. Scanga, P. L. Lin, J. A. L. Flynn, Analysis of 18FDG PET/CT imaging as a tool for studying *Mycobacterium tuberculosis* infection and treatment in non-human primates. *J. Vis. Exp.*, 56375 (2017).
53. C. Jakobs, E. Bartok, A. Kubarenko, F. Bauernfeind, V. Hornung, Immunoblotting for active caspase-1. *Methods Mol. Biol.* **1040**, 103–115 (2013).
54. S. Namasivayam, M. Maiga, W. Yuan, V. Thovarai, D. L. Costa, L. R. Mittereder, M. F. Wipperman, M. S. Glickman, A. Dzutsev, G. Trinchieri, A. Sher, Longitudinal profiling reveals a persistent intestinal dysbiosis triggered by conventional anti-tuberculosis therapy. *Microbiome* **5**, 71 (2017).
55. J. G. Caporaso, J. Kuczynski, J. Stombaugh, K. Bittinger, F. D. Bushman, E. K. Costello, N. Fierer, A. G. Peña, J. K. Goodrich, J. I. Gordon, G. A. Huttley, S. T. Kelley, D. Knights, J. E. Koenig, R. E. Ley, C. A. Lozupone, D. McDonald, B. D. Muegge, M. Pirrung, J. Reeder,

- J. R. Sevinsky, P. J. Turnbaugh, W. A. Walters, J. Widmann, T. Yatsunenko, J. Zaneveld, R. Knight, QIIME allows analysis of high-throughput community sequencing data. *Nat. Methods* **7**, 335–336 (2010).
56. C. Quast, E. Pruesse, P. Yilmaz, J. Gerken, T. Schweer, P. Yarza, J. Peplies, F. O. Glöckner, The SILVA ribosomal RNA gene database project: Improved data processing and web-based tools. *Nucleic Acids Res.* **41**, D590–D596 (2013).
57. N. Segata, J. Izard, L. Waldron, D. Gevers, L. Miropolsky, W. S. Garrett, C. Huttenhower, Metagenomic biomarker discovery and explanation. *Genome Biol.* **12**, R60 (2011).
58. K. D. Mayer-Barber, B. B. Andrade, S. D. Oland, E. P. Amaral, D. L. Barber, J. Gonzales, S. C. Derrick, R. Shi, N. P. Kumar, W. Wei, X. Yuan, G. Zhang, Y. Cai, S. Babu, M. Catalfamo, A. M. Salazar, L. E. Via, C. E. Barry III, A. Sher, Host-directed therapy of tuberculosis based on interleukin-1 and type I interferon crosstalk. *Nature* **511**, 99–103 (2014).
59. J. Rousou, D. D. Agranoff, O. Sodeinde, J. Shawe-Taylor, D. Fernandez-Reyes, Biomarker discovery by sparse canonical correlation analysis of complex clinical phenotypes of tuberculosis and malaria. *PLOS Comput. Biol.* **9**, e1003018 (2013).

Acknowledgments: We are grateful to R. Rao Amara for advice regarding dosing regimen of α PD-1. We thank N. Zhu, D. Stephany, and all staff members of the NIAID, Comparative Medicine Branch (CMB) ABSL3 facility for their technical support. **Funding:** This work was supported by the IRP of the NIAID. G.J.F. is supported by P01AI056299 and R37AI112787. Z.Y. was supported by BCBB Support Services Contract HHSN316201300006W/HHSN27200002.

Author contributions: K.D.K. led the study, performed experiments, analyzed data, and wrote the paper. S.S., N.E.L., T.W.F., and C.E.N. performed experiments and analyzed data. A. Sher and S.N. performed microbiota analysis. K.D.M.-B. and P.J.B. performed Western blot analysis. O.K. performed live imaging studies. D.O.-d.-S., C.L.V., and B.B.A. performed statistical analysis. Z.Y. generated Python script for imaging analysis. C.S.L.A., A. Sette, and G.J.F. provided necessary reagents to perform experiments. R.M. provided veterinary care for infected animals under

ABSL3 conditions. The NIAID/DIR Tuberculosis Imaging Program performed animal manipulations and PET-CT imaging. J.K. performed analysis of imaging data. L.E.V. and T.B.I.P. led PET-CT imaging studies, animal manipulations, animal infections, and necropsies. D.L.B. conceived the study, analyzed data, and wrote the paper. **Competing interests:** D.L.B. has patents on the PD-1/PD-1 pathway. G.J.F. has patents on the PD-1/PD-L1 pathway and pending royalties from Roche, Merck MSD, Bristol-Myers-Squibb, Merck KGA, Boehringer-Ingelheim, AstraZeneca, Dako, Leica, Mayo Clinic, and Novartis. G.J.F. has served on advisory boards for Roche, Bristol Myers Squibb, Xios, Origimed, Triursus, iTeos, NextPoint, IgM, Jubilant, and GV20. G.J.F. has equity in Nextpoint, Triursus, Xios, iTeos, IgM, and GV20. **Data and materials availability:** The 16S rRNA sequencing data are available in the NCBI Short Read Archive database under BioProject ID PRJNA680803. All other data needed to evaluate the conclusions in the paper are present in the paper or the Supplementary Materials. The members of the NIAID/DIR Tuberculosis Imaging Program are Janard L. Bleach, Ashley L. Butler, Emmuanual K. Dayao, Joel D. Fleegle, Felipe Gomez, Michaela K. Piazza, Katelyn M. Repoli, Becky Y. Slone, Michelle K. Sutphin, Laura E. Via, April M. Walker, Danielle M. Weiner, and Michael J. Woodcock.

Submitted 22 October 2020

Accepted 10 December 2020

Published 15 January 2021

10.1126/sciimmunol.abf3861

Citation: K. D. Kauffman, S. Sakai, N. E. Lora, S. Namasivayam, P. J. Baker, O. Kamenyeva, T. W. Foreman, C. E. Nelson, D. Oliveira-de-Souza, C. L. Vinhaes, Z. Yaniv, C. S. Lindestam Arleham, A. Sette, G. J. Freeman, R. Moore, NIAID/DIR Tuberculosis Imaging Program, A. Sher, K. D. Mayer-Barber, B. B. Andrade, J. Kabat, L. E. Via, D. L. Barber, PD-1 blockade exacerbates *Mycobacterium tuberculosis* infection in rhesus macaques. *Sci. Immunol.* **6**, eabf3861 (2021).

PD-1 blockade exacerbates *Mycobacterium tuberculosis* infection in rhesus macaques

Keith D. Kauffman, Shunsuke Sakai, Nickiana E. Lora, Sivaranjani Namasivayam, Paul J. Baker, Olena Kamenyeva, Taylor W. Foreman, Christine E. Nelson, Deivide Oliveira-de-Souza, Caian L. Vinhaes, Ziv Yaniv, Cecilia S. Lindestam Arleham, Alessandro Sette, Gordon J. Freeman, Rashida Moore, NIAID/DIR Tuberculosis Imaging Program, Alan Sher, Katrin D. Mayer-Barber, Bruno B. Andrade, Juraj Kabat, Laura E. Via and Daniel L. Barber

Sci. Immunol. **6**, eabf3861.
DOI: 10.1126/sciimmunol.abf3861

PD-1 blockade carries perils

The potentiation of T cell–mediated antitumor responses achieved in multiple types of cancer via inhibition of the PD-1 checkpoint pathway has led to suggestions that anti–PD-1 therapy might also boost T cell immunity in chronic infections including tuberculosis. Kauffman *et al.* examined the effect of anti–PD-1 antibody treatment on the clinical course of *Mycobacterium tuberculosis* (Mtb) infection in rhesus macaques. CD8 T cell responses were boosted in monkeys receiving anti–PD-1 infusions, but the stronger CD8 T cell responses were coupled with increases in proinflammatory cytokines, impaired CD4 T cell function, and higher bacterial loads in lung granulomas. These findings in a nonhuman primate model signal that anti –PD-1–based therapy needs to be used cautiously in patients with cancer with a history of Mtb exposure.

ARTICLE TOOLS

<http://immunology.sciencemag.org/content/6/55/eabf3861>

SUPPLEMENTARY MATERIALS

<http://immunology.sciencemag.org/content/suppl/2021/01/11/6.55.eabf3861.DC1>

REFERENCES

This article cites 56 articles, 18 of which you can access for free
<http://immunology.sciencemag.org/content/6/55/eabf3861#BIBL>

PERMISSIONS

<http://www.sciencemag.org/help/reprints-and-permissions>

Use of this article is subject to the [Terms of Service](#)

Science Immunology (ISSN 2470-9468) is published by the American Association for the Advancement of Science, 1200 New York Avenue NW, Washington, DC 20005. The title *Science Immunology* is a registered trademark of AAAS.

Copyright © 2021 The Authors, some rights reserved; exclusive licensee American Association for the Advancement of Science. No claim to original U.S. Government Works